

Three-dimensional interaction of thermoacoustic modes in a circular tube

Weipeng Zhou¹, Xiaoyu Wang¹, Guangyu Zhang¹, Maria Heckl², Xiaofeng Sun³

1. Research Institute of Aero-engine, Beihang University, Beijing 10091, China

2. School of Chemical and Physical Sciences, Keele University, Staffordshire ST5 5GB, United Kingdom

3. School of Energy and Power Engineering, Beihang University, Beijing 10091, China

Abstract

This study applies the Green's function method to investigate the modal interaction during thermoacoustic instability specifically in the afterburner. The afterburner is modelled as a cylindrical tube with a compact flame. Nonlinear effects are accounted for by employing the flame describing function (FDF). An integral governing equation for the acoustic velocity at the flame is derived. This is solved by an iteration method to obtain the time history of the acoustic velocity at the flame. The coupling mechanism, which is nonlinear due to the amplitude-dependence of the FDF, is explored using a two-mode analysis as an illustrative example. Different scenarios are observed when the initial amplitude is varied: the long-term behaviour of the time history may be dominated by one of the modes, which forms a limit cycle and squeezes out the other mode, i.e. there is a mutually inhibitory effect; however, it is also possible, for both modes to coexist. This dependence on the initial condition is a consequence of the amplitude-dependent heat release rate, and it is clearly a nonlinear effect. The time history calculation is supplemented by a phase analysis, which is based on the Rayleigh criterion and reveals the stability behaviour and limit cycles of the individual modes. In order to simulate changing operating conditions in a real afterburner, the coupling coefficient and the time-lag in the heat release rate are changed abruptly during the time history calculation. The change in coupling coefficient has no dramatic effect, while the change in time-lag can lead to mode switch. This is examined in detail by the phase analysis, which reveals that mode switching is also a nonlinear effect.

Key words: thermoacoustic instability; interaction of multiple modes; nonlinearity; Green's function; time domain.

List of symbols

A : peak value in the time history of u'_q

a : radius of afterburner

c_0 : sound speed

f_{100} : thermoacoustic frequency of mode (1,0,0)

f_{101} : thermoacoustic frequency of mode (1,0,1)

$G(\vec{r}, \vec{r}', t - t')$: Green's function

G_{mnk} : gradient of the Green's function amplitude

g_{mnk} : amplitude of Green's function mode (m, n, k)

J_m : Bessel function of first kind.

j : imaginary unit

K : heat power per unit mass flow

k_{mm} : radial wavenumber

L : length of afterburner

m, n, k : circumferential, radial and axial mode numbers, respectively.

\vec{n} : unit normal vector to the flame surface

n_0, n_1 : interaction indices of the flame describing function

p' : acoustic pressure

Q' : global heat release rate

q' : local heat release rate

$\vec{r}_q = (r_q, \varphi_q, z_q)$: position of the flame

$\vec{r} = (r, \varphi, z)$: observer position

$\vec{r}' = (r', \varphi', z')$: position of a hypothetical point source

$S_{pq}(f)$: Fourier coefficients of the cross-spectrum of $p'(t)$ and $q'(t)$

s : variable of Laplace transform

t : observer time

t' : time when the source emits signal

u'_q : velocity component normal to the flame surface

u'_{q1} : acoustic velocity related to mode (1,0,0)

u'_{q2} : acoustic velocity related to mode (1,0,1)

δ : Dirac's delta function

ε_k : a constant that takes values of either 1 or 2.

θ_f : elevation angle of the normal vector to the flame surface

ρ : density

τ : delay time

τ_0, τ_1, g_0, g_1 : constants that determine the flame describing function

Φ_f : azimuth angle of the normal vector to the flame surface

ϕ : velocity potential

ϕ_0 : initial velocity potential at the flame

$\phi_{pq}(f)$: relative phase angle between p' and q'

ω_{mnk} : natural angular frequency of mode (m, n, k)

Overbars denote the mean part of field quantities, primes denote the fluctuating part of field quantities in the time-domain, and hats denote the fluctuating part of field quantities in the frequency-domain. The time dependence of a quantity oscillating with frequency ω is denoted by $e^{j\omega t}$.

1. Introduction

Thermoacoustic instability is a prevalent challenge encountered in various propulsion systems [1-5]. In order to comply with increasingly stringent environmental regulations, particularly concerning NO_x emissions, lean-premixed pre-vaporized (LPP) combustion has been widely implemented [6]. This combustion approach operates with excess air to lower the flame temperature, thus reducing NO_x emissions. However, due to the combustion chamber operating at lean fuel-air mixtures, this shift in combustion strategy has led to an increased susceptibility to thermoacoustic instability [7,8]. Given that the energy density in the combustion chamber is very high, only a small portion of it can drive thermoacoustic oscillations [9,10]. As a consequence, the combustion chamber or even the entire system can experience strong vibrations, resulting in heightened noise and heat loads, and increased pollutant emissions. In severe cases, it can even lead to the failure of the entire combustion system.

The phenomenon of thermoacoustic instability was first observed by Higgins in 1777, using a vertical tube with a hydrogen flame [11]. Subsequently, Rijke replicated thermoacoustic instability by substituting the flame with a hot gauze [12]. The Rijke tube and its improved versions have since become standard equipment for investigating the mechanisms and control techniques of thermoacoustic instability [13]. Much research has been conducted using the Rijke tube to investigate the instability mechanisms [14-16] and active [17-20] and passive control [21-26] of thermoacoustic oscillations. These studies have revealed the mechanisms causing thermoacoustic instabilities and proposed various strategies to effectively suppress these in the Rijke tube. However, due to the simplicity of the Rijke tube apparatus, the thermoacoustic oscillations observed in it differ significantly from those encountered in practical combustion systems. Therefore, it is not always obvious how to adapt the aforementioned control methods to real combustion systems. Consequently, the study of thermoacoustic instabilities in practical combustion systems is necessary. It needs to take into account the following characteristics in order to gain a deeper understanding and develop suppression techniques. Firstly, in modern aircraft engines, the circumferential scale is greater than the axial scale, resulting in the existence of not only axial modes but also circumferential modes, which may be the dominant modes [27-29]. Thus, research on thermoacoustic instability should incorporate the influence of three-dimensional effects. Secondly, due to the high energy density in real-world combustion systems, multiple unstable modes can be simultaneously excited, making the interaction between modes a topic of significant interest [30-34]. Lastly, due to the high amplitudes associated with thermoacoustic instabilities, a nonlinear modelling approach is required [35,36].

With a linear approach, one can only predict the onset of instability of an individual mode, but not the transient behaviour that precedes a limit cycle, nor the (constant) oscillation amplitude once the limit cycle has been reached. When controlling thermoacoustic oscillations, it is not necessary to completely suppress them, but rather to limit their amplitudes to an acceptable range [37]. Therefore, predicting the occurrence of limit cycles has become increasingly important, and research has gradually shifted from linear to nonlinear approaches to investigate limit cycles. These three interconnected issues constitute the complex phenomenon of thermoacoustic oscillations in modern aircraft engines.

In order to study the complex phenomenon of thermoacoustic instability observed in practical aircraft engines, numerous methods have been developed, which can be broadly classified into three categories: experiments, numerical simulations, and analytical methods. Moeck et al. [38] connected twelve Rijke tubes to an annular duct to simulate a practical annular combustion chamber and to study azimuthal modes found in modern engines. Their experimental results show that two coexisting circumferential unstable modes exist in the system, alternating in dominance as the heating power changes. Introducing asymmetry into the system can increase stability but may also lead to mode degeneration. The research group at the EM2C Laboratory has developed a combustion test-rig called MICCA [39-43], which allows the investigation of various modes in a multiple-injector annular combustor. Yuanqi Fang et al. [44,45] developed a combustion chamber, called TurboCombo, based on the MICCA combustor, in order to study the interaction between various mode structures. They discovered an "intermittent switching behavior" between the quarter-wavelength longitudinal mode in the combustion chamber and the first-order azimuthal mode in the static pressure chamber. The system's limit cycle randomly switches between these two modes.

Numerical simulations of combustion can be categorized into three main types based on increasing computational cost: Reynolds-averaged Navier-Stokes simulation (RANS) [46,47], large-eddy simulation (LES), and direct numerical simulation (DNS) [48,49]. Their advantage lies in their ability to accurately simulate the geometric shape of practical combustion systems, thereby directly incorporating the influence of three-dimensional effects. The challenge in numerical simulations lies in handling the coexistence of multiple length scales within the system. RANS requires various models for Reynolds stresses to close the equations. Although RANS may be suitable for time-averaged turbulent flow properties, its validity for capturing unsteady flow evolution, especially in complex configurations such as swirling flows with recirculation, remains uncertain. DNS, the most precise method due to its requirement to resolve all scales, incurs substantial computational costs, limiting its application to small

computational domains rather than practical engineering systems [50]. By comparison, LES is widely employed in researching thermoacoustic instability. Gicquel et al. [51] used LES to simulate the flame in a gas turbine's combustion chamber, aiming to describe the unsteady heat release through numerical simulations. The results indicated that all nozzles in the annular combustion chamber had identical flame transfer functions. Boudier et al. [52] analyzed thermoacoustic stability in a helicopter gas turbine combustor using LES, verifying the consistency between LES and a Helmholtz solver and identifying possible unstable modes within the combustion chamber. The LIMOUSINE project (Limit Cycles of Thermo-Acoustic Oscillations in Gas Turbine Combustors), funded by the European Union, employed LES to simulate aerodynamic coupling and combustion transients, thereby establishing mathematical models for liquid fuel combustion [53-55].

Experimental investigations suffer from complexity, expense, and time requirements, while numerical simulations demand substantial computational resources and time. In cases where the understanding of physical mechanisms is a priority, or the influence of multiple parameters is to be studied, analytical models become the method of choice. Theoretical methods have made significant progress in this regard. Network methods, which operate in the frequency domain and solve for complex eigenfrequencies, play a crucial role. These methods divide the system into simple sub-elements and connect them through jump conditions, incorporating heat release models and boundary conditions, to obtain the dispersion relation equations for studying stability, limit cycles and so on. Various complex models have been developed based on this approach. Parmentier et al. [56] utilized a one-dimensional analytical theory based on the network model to study azimuthal modes, demonstrating good agreement between the complex eigenfrequencies obtained through this method and a full three-dimensional Helmholtz solver. They also showed that symmetry breaking had a beneficial effect on stability. The network model was extended to simulate more complex geometries, including upstream plenums, downstream chambers and multiple burners, in order to investigate the coupling between these elements [57]. Evesque et al. [58] developed a two-dimensional low-order model for mode coupling; by solving the dispersion relation equation, they were able to predict the frequencies, mode shapes, and stability behaviour of the combustion system. You et al. [59] established a three-dimensional thermoacoustic instability model based on the mode-matching method. The method can account for the non-uniformity of the flow velocity within the combustion chamber, thereby capturing higher-order modes that include circumferential and radial components, making it more representative of a real combustion chamber. Later, Li and Sun [60] developed a three-dimensional analytical method to investigate the effect of vorticity waves on

azimuthal instabilities in annular combustion chambers and demonstrated that the results for the pure azimuthal mode with vorticity disturbance are significantly different from those without. Guangyu Zhang [61] developed a three-dimensional analytical model, which includes perforated liners on both the inner and outer walls of an annular combustion chamber, to study the effect of acoustic liners on thermoacoustic instability. In order to investigate the coupling mechanisms between modes, Moeck [32] studied the interaction of modes within the framework of harmonic balance. The results demonstrated that the coupling between different modes had a mutually suppressing effect. Bigongiari and Heckl [62] utilized the Green's function method to study the interaction between modes, revealing that if this method was applied in the frequency domain, it failed to predict which modes are dominant. However, both of the aforementioned studies were conducted under the assumption of basic one-dimensional behavior, where only longitudinal acoustic waves were present in the system. In order to investigate the interaction between different modal structures in three dimensions, this study extends the Green's function method to *three* dimensions. Nonlinear flame transfer functions were also employed in the calculations to investigate the characteristics of limit cycles when three-dimensional multi-mode interaction occurs. The work reported in the current paper is unique because it focuses on the following open research questions:

1. **Incorporation of Three-Dimensional Effects:** In modern aircraft engines, the circumferential scale surpasses the axial scale, introducing not only axial modes but also dominant circumferential modes. Our study acknowledges and incorporates the influence of three-dimensional effects in a cylindrical combustion chamber (the prototype of an afterburner), providing a more comprehensive understanding of thermoacoustic instability.
2. **Interaction Between Multiple Unstable Modes:** Recognizing the high energy density in actual combustion systems, our research acknowledges the simultaneous excitation of multiple unstable modes. The investigation of the interaction between these modes sheds light on their complexity and provides insights crucial for suppressing thermoacoustic oscillations effectively.
3. **Focus on Limit Cycles and Nonlinear Approaches:** Traditional linear analyses predict exponential growth of amplitude over time in thermoacoustic oscillations. However, our study emphasizes the recently heightened attention on limit cycles, where oscillations reach a constant amplitude due to nonlinear effects. By shifting from linear to nonlinear approaches, we provide novel physical insight that will aid in predicting and controlling thermoacoustic oscillations.

Moreover, in contrast to most existing models, which are in the frequency domain, our model gives the *time*

history of the acoustic velocity, thereby providing a visual representation of the stability behaviour and limit cycles. This paper is structured as follows: Section 2 describes the methods employed in this study. The results obtained in the frequency domain (Section 3.1) and the time domain (Section 3.2) are presented and subsequently analyzed (Sections 3.2.1 and 3.2.2, respectively). Section 3.3 showcases an intriguing phenomenon called "mode switch." Finally, conclusions are drawn in Section 4.

2. Method

In order to investigate the phenomenon of multi-mode interaction of thermoacoustic oscillations occurring in gas turbines, specifically in the afterburner, we have developed a simplified geometric model. As illustrated in Fig. 1, the model consists of a circular tube with radius a and length L .

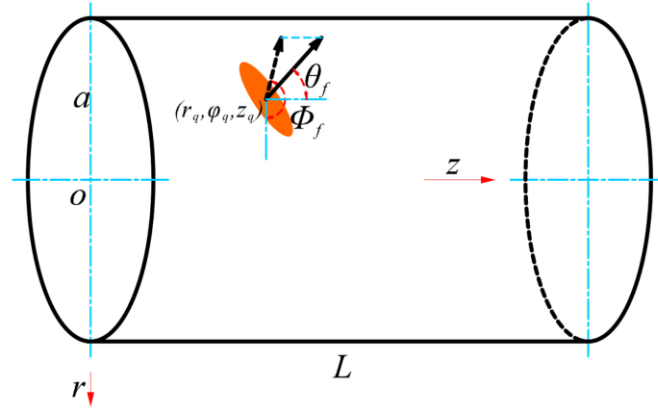


Fig. 1. Idealised geometry representing an afterburner. The cylindrical tube has length L and radius a . The combustion takes place in a small flame surface, which is located at position $\vec{r}_q = (r_q, \varphi_q, z_q)$ and has surface normal \vec{n} .

The flame is assumed to be compact and represented by a small flame surface positioned at $\vec{r}_q = (r_q, \varphi_q, z_q)$ within the circular tube. The normal direction of the flame surface is determined by the azimuth Φ_f and the elevation angle θ_f . Our model assumes a uniform temperature distribution and neglects the mean flow.

Both the inlet boundary (connection to turbine outlet) and outlet boundary (connection to atmosphere) are treated as acoustically closed ends, to simulate choked flow, i.e., the condition where the gas flow through the ends reaches the speed of sound.

2.1 The tailored Green's function for the idealised geometry

The Green's function describes the acoustic field produced by a hypothetical point source. $G(\vec{r}, \vec{r}', t-t')$ denotes the Green's function in this paper, where \vec{r}' is the location of the point source with $\vec{r}' = (r', \varphi', z')$, \vec{r} is the location of an observer with $\vec{r} = (r, \varphi, z)$, and $t-t'$ is the time it takes for the sound signal to travel from \vec{r}' to \vec{r} . The governing equation for $G(\vec{r}, \vec{r}', t-t')$ is the nonhomogeneous wave equation

$$\frac{1}{c_0^2} \frac{\partial^2 G}{\partial t^2} - \nabla^2 G = \delta(\vec{r} - \vec{r}') \delta(t-t'), \quad (1)$$

where c_0 denotes the sound speed and δ denotes Dirac's delta function. With the assumption that the ends and the wall of the cylindrical tube are hard, we can write the boundary condition as

$$\frac{\partial G}{\partial \vec{r}} = 0. \quad (2)$$

The Green's function, which also satisfies Eq. (2) is called the "tailored Green's function". It is given by

$$G(\vec{r}, \vec{r}', t-t') = \sum_m \sum_n \sum_k g_{mnk}(\vec{r}, \vec{r}') \left(\frac{e^{j\omega_{mnk}(t-t')}}{2} - \frac{e^{-j\omega_{mnk}(t-t')}}{2} \right), \quad (3)$$

where

$$g_{mnk}(\vec{r}, \vec{r}') = c_0^2 \frac{J_m(k_{mn}r) e^{jm\varphi} \cos\left(\frac{k\pi}{L}z\right) J_m(k_{mn}r') e^{-jm\varphi'} \cos\left(\frac{k\pi}{L}z'\right)}{j\omega_{mnk} \frac{\pi L}{\varepsilon_k} \left(r^2 - \frac{m^2}{k_{mn}^2}\right) J_m^2(k_{mn}r) \Big|_{r=0}^{r=a}}, \quad (4)$$

with

$$\omega_{mnk} = c_0 k_0, \quad (5)$$

and

$$k_0 = \sqrt{k_{mn}^2 + \left(\frac{k\pi}{L}\right)^2}. \quad (6)$$

j is the imaginary unit. m, n, k denote the circumferential, radial, and axial mode numbers, respectively. ω_{mnk} is the natural angular frequency of mode (m, n, k) , J_m denotes the Bessel function of the first kind and order m . k_{mn} represents the radial wavenumber, which is the $(n+1)$ -th solution of Eq. (A.35). Once the value of k_{mn} is obtained, we can use Eq. (6) to determine the value of k_0 , and subsequently calculate ω_{mnk} from Eq. (5). The term ε_k is defined by

$$\varepsilon_k = \begin{cases} 1 & \text{if } m=0 \\ 2 & \text{if } m>0 \end{cases} \quad (7)$$

The detailed derivation of Green's function for the cylindrical geometry is provided in Appendix A.

2.2 The nonlinear heat release model

This paper is a model-based study, focusing on using a nonlinear heat release model to investigate the coupling mechanisms between modes under nonlinear conditions, rather than capturing the unsteady heat release in a real afterburner. Therefore, a simplified flame describing function (FDF) is employed to characterize the flame. It is assumed that the heat source is compact, located at \vec{r}_q , and the following relationship between the oscillating heat release rate, Q' , and the velocity component u'_q perpendicular to the flame surface [63] is adopted:

$$\begin{aligned} \text{time domain: } \frac{Q'(t)}{\bar{Q}} &= n_1 \frac{u'_q(t-\tau)}{\bar{u}_q} - n_0 \frac{u'_q(t)}{\bar{u}_q}, \\ \text{frequency domain: } \frac{\hat{Q}(\omega)}{\bar{Q}} &= (n_1 e^{-j\omega\tau} - n_0) \frac{\hat{u}_q(\omega)}{\bar{u}_q}, \end{aligned} \quad (8)$$

where the overbar denotes the time-mean component, and the prime denotes the fluctuating component. The equivalent expressions of Eq. (8) for the local heat release rate q' and \hat{q} , are given by

$$\begin{aligned} \text{time domain: } q'(\vec{r}, t) &= K [n_1 u'_q(t-\tau) - n_0 u'_q(t)] \delta(\vec{r} - \vec{r}_q), \\ \text{frequency domain: } \hat{q}(\vec{r}, \omega) &= K [n_1 e^{-j\omega\tau} - n_0] \hat{u}_q(\omega) \delta(\vec{r} - \vec{r}_q), \end{aligned} \quad (9)$$

where $K = \frac{\bar{Q}}{\bar{u}_q S \rho}$ is the heat power per unit mass flow. The expressions for the interaction indices n_1 , n_0 and the

delay time τ are given by

$$\tau = \tau_0 + \tau_1 \left(\frac{A}{\bar{u}_q} \right)^2, \quad g = g_0 - g_1 \frac{A}{\bar{u}_q}, \quad n_0 = \frac{g-1}{2}, \quad n_1 = \frac{g+1}{2}. \quad (10)$$

τ_0 , τ_1 , g_0 , g_1 are constants, which characterise the flame dynamics. This FDF has been adopted extensively in nonlinear research of thermoacoustic instabilities, and it has been demonstrated that it captures the phenomena of limit cycle and hysteresis. Additionally, this FDF has a simple form and can be easily applied to a variety of combustion devices by selecting appropriate parameters. We therefore use it for our research on coupling of modes.

The values $\tau_0 = 5 \times 10^{-3}$ s, $\tau_1 = 4.4 \times 10^{-3}$ s, $g_0 = 1.4$, $g_1 = 0.3$ are adopted here, following the choice in [64]. A is

the peak value of the total oscillating velocity $\overline{u'_q}$ perpendicular to the flame surface.

2.3 The integral governing equation

The velocity potential generated by the heat source can be described by the acoustic analogy equation

$$\frac{1}{c_0^2} \frac{\partial^2 \phi}{\partial t^2} - \nabla^2 \phi = -\frac{\gamma-1}{c_0^2} q'(\vec{r}, t). \quad (11)$$

The considered cylinder has a hard wall and hard ends, therefore, the boundary condition is the same as that for the tailored Green's function,

$$\frac{\partial \phi}{\partial \vec{r}} = 0. \quad (12)$$

The following initial conditions are assumed for the convenience of calculation:

$$\phi|_{t=0} = \phi_0 \delta(\vec{r} - \vec{r}_q), \quad \frac{\partial \phi}{\partial t}|_{t=0} = 0. \quad (13)$$

Eqs. (1) and (11) can be combined, and after several mathematical steps, converted into the following integral equation for the velocity potential,

$$\phi(\vec{r}, t) = -\frac{\gamma-1}{c_0^2} \iint G(\vec{r}, \vec{r}', t-t') q'(\vec{r}', t') d\vec{r}' dt' - \frac{\phi_0}{c_0^2} \left(\frac{\partial G}{\partial t'} \right) \Big|_{t'=0, \vec{r}'=\vec{r}_q}. \quad (14)$$

The detailed derivation is shown in Appendix B. An equation for the acoustic velocity at the heat source can be obtained by differentiating Eq. (14) with respect to the flame surface normal \vec{n} and then evaluating the result at $\vec{r} = \vec{r}_q$,

$$u'_q(t) = \frac{\partial \phi(\vec{r}, t)}{\partial \vec{n}} \Big|_{\vec{r} = \vec{r}_q} = -\frac{\gamma-1}{c_0^2} \int_0^t \frac{\partial G(\vec{r}, \vec{r}', t-t')}{\partial \vec{n}} \Big|_{\substack{\vec{r}=\vec{r}_q \\ \vec{r}'=\vec{r}_q}} q'(t') dt' - \frac{\phi_0}{c_0^2} \left(\frac{\partial^2 G}{\partial \vec{n} \partial t'} \right) \Big|_{\substack{t'=0 \\ \vec{r}'=\vec{r}_q}}, \quad (15)$$

where the derivative with respect to \vec{n} is given by

$$\frac{\partial}{\partial \vec{n}} = (\cos \Phi_f \sin \theta_f \cos \varphi + \sin \Phi_f \sin \theta_f \sin \varphi) \frac{\partial}{\partial r} + (\sin \Phi_f \sin \theta_f \cos \varphi - \cos \Phi_f \sin \theta_f \sin \varphi) \frac{1}{r} \frac{\partial}{\partial \varphi} + \cos \theta_f \frac{\partial}{\partial z}. \quad (16)$$

With the abbreviation

$$G_{mnk} = \left. \frac{\partial g_{mnk}(\vec{r}, \vec{r}')}{\partial \vec{n}} \right|_{\substack{\vec{r}=\vec{r}_q \\ \vec{r}'=\vec{r}_q}}, \quad (17)$$

and Eq. (3), we can write the last term in Eq. (15) as

$$\left(\frac{\partial^2 G}{\partial n \partial t'} \right) \Big|_{\substack{t'=0 \\ \vec{r}=\vec{r}_q \\ \vec{r}'=\vec{r}_q}} = \sum_{m,n,k=0}^{\infty} G_{mnk} \frac{1}{2} j \omega_{mnk} (-e^{j\omega_{mnk}t} - e^{-j\omega_{mnk}t}) = - \sum_{m,n,k=0}^{\infty} G_{mnk} j \omega_{mnk} \cos(\omega_{mnk}t), \quad (18)$$

and Eq. (15) becomes

$$u_q'(t) = -\frac{\gamma-1}{c_0^2} \int_0^t \sum_{m,n,k=0}^{\infty} G_{mnk} \left[\frac{e^{j\omega_{mnk}(t-t')}}{2} - \frac{e^{-j\omega_{mnk}(t-t')}}{2} \right] q'(t') dt' \\ + \frac{\phi_0}{c_0^2} \sum_{m,n,k=0}^{\infty} G_{mnk} j \omega_{mnk} \cos(\omega_{mnk}t). \quad (19)$$

2.4 The solution of the integral governing equation

Eq. (19) describes the evolution of the sound field inside the cylindrical tube generated by thermoacoustic feedback. It is an integral equation for the velocity $u_q'(t)$, which appears on the left-hand side, and also inside the integral. Two different methods are introduced to solve this equation: the first is the derivation (based on the Laplace transform) of an algebraic equation for the complex eigenfrequency; the second is a numerical iteration method that gives the time history of the acoustic velocity.

2.4.1 Laplace transform method

The Laplace transform is applied to both sides of Eq. (19), yielding

$$\hat{u}_q(s) = -c_q \sum_{m,n,k=0}^{\infty} G_{mnk} \frac{1}{2} \left(\frac{1}{s - j\omega_{mnk}} - \frac{1}{s + j\omega_{mnk}} \right) (n_1 e^{-s\tau} - n_0) \hat{u}_q(s) \\ + \frac{\phi_0}{c_0^2} \sum_{m,n,k=0}^{\infty} G_{mnk} j \omega_{mnk} \frac{1}{2} \left(\frac{1}{s - j\omega_{mnk}} + \frac{1}{s + j\omega_{mnk}} \right), \quad (20)$$

where the abbreviation

$$c_q = \frac{\gamma-1}{c_0^2} K \quad (21)$$

has been introduced. Eq. (20) can be solved for $\hat{u}_q(s)$ to give

$$\hat{u}_q(s) = \frac{\frac{\phi_0}{c_0^2} \sum_{m,n,k=0}^{\infty} G_{mnk} j\omega_{mnk} \frac{1}{2} \left(\frac{1}{s - j\omega_{mnk}} + \frac{1}{s + j\omega_{mnk}} \right)}{\left[1 + c_q \sum_{m,n,k=0}^{\infty} G_{mnk} \frac{1}{2} \left(\frac{1}{s - j\omega_{mnk}} - \frac{1}{s + j\omega_{mnk}} \right) (n_1 e^{-s\tau} - n_0) \right]} \quad (22)$$

In order to obtain the expression in the *time* domain, the inverse Laplace transform is applied to both sides of Eq. (22), and the resulting integral is evaluated with the residue theorem. The residue theorem requires the denominator of Eq. (22) to be zero and the following equation for the complex eigenfrequency Ω can be obtained:

$$1 = -c_q \sum_{m,n,k=0}^{\infty} G_{mnk} \frac{1}{2} \left(\frac{1}{s - j\omega_{mnk}} - \frac{1}{s + j\omega_{mnk}} \right) (n_1 e^{-s\tau} - n_0), \quad (23)$$

where $s = j\Omega$. It can be solved by Newton's iterative method. The real part of Ω gives the thermoacoustic oscillation frequency, while the imaginary part of Ω gives the growth rate. When $\text{Im}(\Omega) > 0$, the system is stable; when $\text{Im}(\Omega) < 0$, the system is unstable with the time dependence $e^{j\Omega t}$.

2.4.2 Numerical iteration method

The numerical iteration method described by Heckl and Howe [65] is adopted. We define two integrals as shown in Eq. (24) below, and divide the integration range into two parts: $t'=0 \dots t-\Delta t$ and $t'=t-\Delta t \dots t$, where the second part is a very short time interval of duration Δt .

$$\begin{aligned} I_{mnk1}(t) &= \int_{t'=0}^{t'=t} \frac{e^{-j\omega_{mnk}t'}}{2} q'(t') dt' = \int_{t'=0}^{t'=t-\Delta t} \frac{e^{-j\omega_{mnk}t'}}{2} q'(t') dt' + \int_{t'=t-\Delta t}^{t'=t} \frac{e^{-j\omega_{mnk}t'}}{2} q'(t') dt', \\ I_{mnk2}(t) &= \int_{t'=0}^{t'=t} \frac{e^{j\omega_{mnk}t'}}{2} q(t') dt' = \int_{t'=0}^{t'=t-\Delta t} \frac{e^{j\omega_{mnk}t'}}{2} q(t') dt' + \int_{t'=t-\Delta t}^{t'=t} \frac{e^{j\omega_{mnk}t'}}{2} q(t') dt'. \end{aligned} \quad (24)$$

$q'(t')$ is assumed to be constant in the very short time interval Δt , yielding

$$\begin{aligned} I_{mnk1}(t) &= I_{mnk1}(t-\Delta t) + \frac{q'(t-\Delta t) e^{-j\omega_{mnk}t} (1 - e^{j\omega_{mnk}\Delta t})}{2(-j\omega_{mnk})}, \\ I_{mnk2}(t) &= I_{mnk2}(t-\Delta t) + \frac{q'(t-\Delta t) e^{j\omega_{mnk}t} (1 - e^{-j\omega_{mnk}\Delta t})}{2(j\omega_{mnk})}. \end{aligned} \quad (25)$$

Substituting Eqs. (25) and (18) into Eq. (19), we get

$$u_q'(t) = -\frac{\gamma-1}{c^2} \sum_{m,n,k=0}^{\infty} G_{mnk} [e^{j\omega_{mnk}t} I_{mnk1}(t) - e^{-j\omega_{mnk}t} I_{mnk2}(t)] - \frac{\phi_0}{c^2} \sum_{m,n,k=0}^{\infty} G_{mnk} \frac{1}{2} j\omega_{mnk} (-e^{j\omega_{mnk}t} - e^{-j\omega_{mnk}t}). \quad (26)$$

We will solve this equation in Section 3.2 by iteration (using a straightforward time-stepping procedure) to obtain

the time history of the acoustic velocity. During this iteration, the peak value A is updated every time a maximum occurs in the time history of the total velocity $u_q'(t)$.

3. Results

In practical afterburners, it is common to observe multiple modes simultaneously. The interaction between these modes has a significant impact on the stability behavior of the system and any limit cycles that might occur. The methods described in Section 2 of this paper are employed to examine the coupling mechanism between modes. Specifically, our investigation focuses on two prominent modes, namely (1,0,0) and (1,0,1), which are known to be the most easily excited and unstable thermoacoustic modes in real-world applications. The first number represents the circumferential mode number, the second number represents the radial mode number, and the third number represents the axial mode number. The parameter values used for the analysis are given in Table 1.

Table 1. Parameter values for the analysis

L/m	a/m	c_0/ms^{-1}	$K/\text{W}\cdot\text{s}\cdot\text{kg}^{-1}$	r_q/m	φ_q	z_q/m	Φ_f	θ_f
2	0.5	340	14500	0.25	$\pi/4$	0.465	$\pi/4$	$\pi/3$

These parameters describe an idealised afterburner in terms of the cylindrical setup shown in Fig. 1. The cylinder has length $L = 2$ m and radius $a = 0.5$ m. The fluid inside the cylinder is air at room temperature, and the corresponding speed of sound is $c_0 = 340$ ms^{-1} . The heat source is a small surface positioned at the point $r_q = 0.25$ m, $\varphi_q = \pi/4$, $z_q = 0.465$ m, and the orientation of the surface is given by the angles $\theta_f = \pi/3$ and $\Phi_f = \pi/4$. The thermal power per unit mass flow of the heat source is $K = 14500$ $\text{W}\cdot\text{s}\cdot\text{kg}^{-1}$.

3.1 Results in the frequency domain

In this section, we present frequency-domain results obtained by solving Eq. (23). Fig. 2 presents the results for the complex eigenfrequencies Ω as a function of the peak value A/\bar{u}_q .

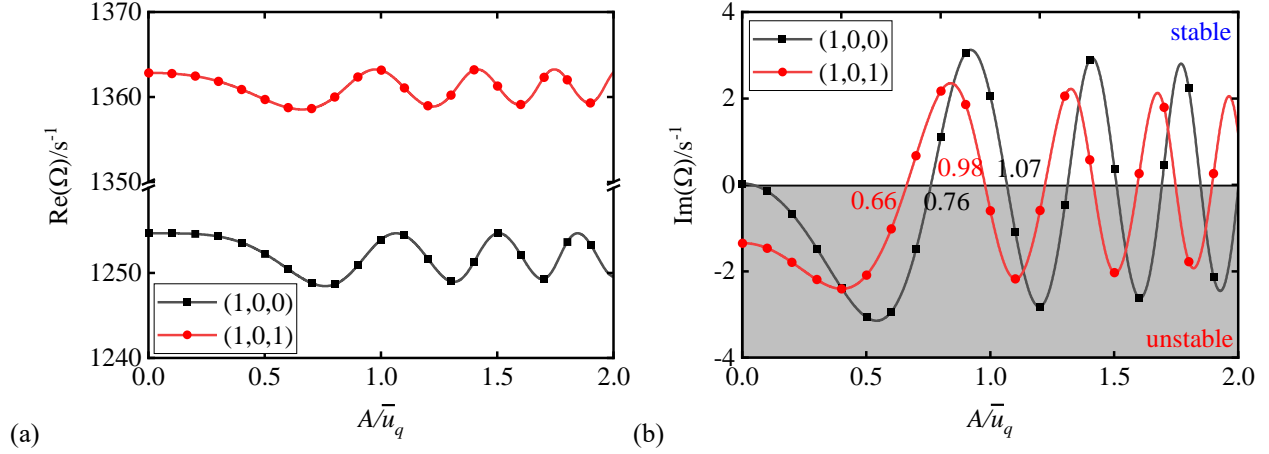


Fig. 2. Complex eigenfrequencies Ω predicted by the Laplace method; A/\bar{u}_q is the dimensionless peak value. (a) real part of Ω , (b) imaginary part of Ω ; the grey shading marks the region of instability.

Fig. 2a illustrates the thermoacoustic oscillation frequencies $\text{Re}(\Omega_{100})$ and $\text{Re}(\Omega_{101})$, which fluctuate around the frequencies of the Green's function modes $\omega_{100} = 1251.88\text{s}^{-1}$ and $\omega_{101} = 1361.04\text{s}^{-1}$, respectively. Fig. 2b shows the corresponding growth rates. According to Fig. 2b, both modes are unstable when the initial velocity A/\bar{u}_q is small (below about 0.6). Mode (1,0,1) stabilises after reaching an amplitude of 0.66, while mode (1,0,0) remains unstable until the amplitude reaches 0.76. These results give no information on any interaction between the modes, or on the long-term behaviour (such as limit cycles) of the two modes. We therefore continue our analysis in the time domain.

3.2 Results in the time domain

In this section, we present time-domain results obtained by the numerical iteration method based on Eq. (26). These are shown in Figs. 3, 4 and 5, for three different initial velocity amplitudes, respectively: $A/\bar{u}_q = 0.01$, 0.5 and 1.1.

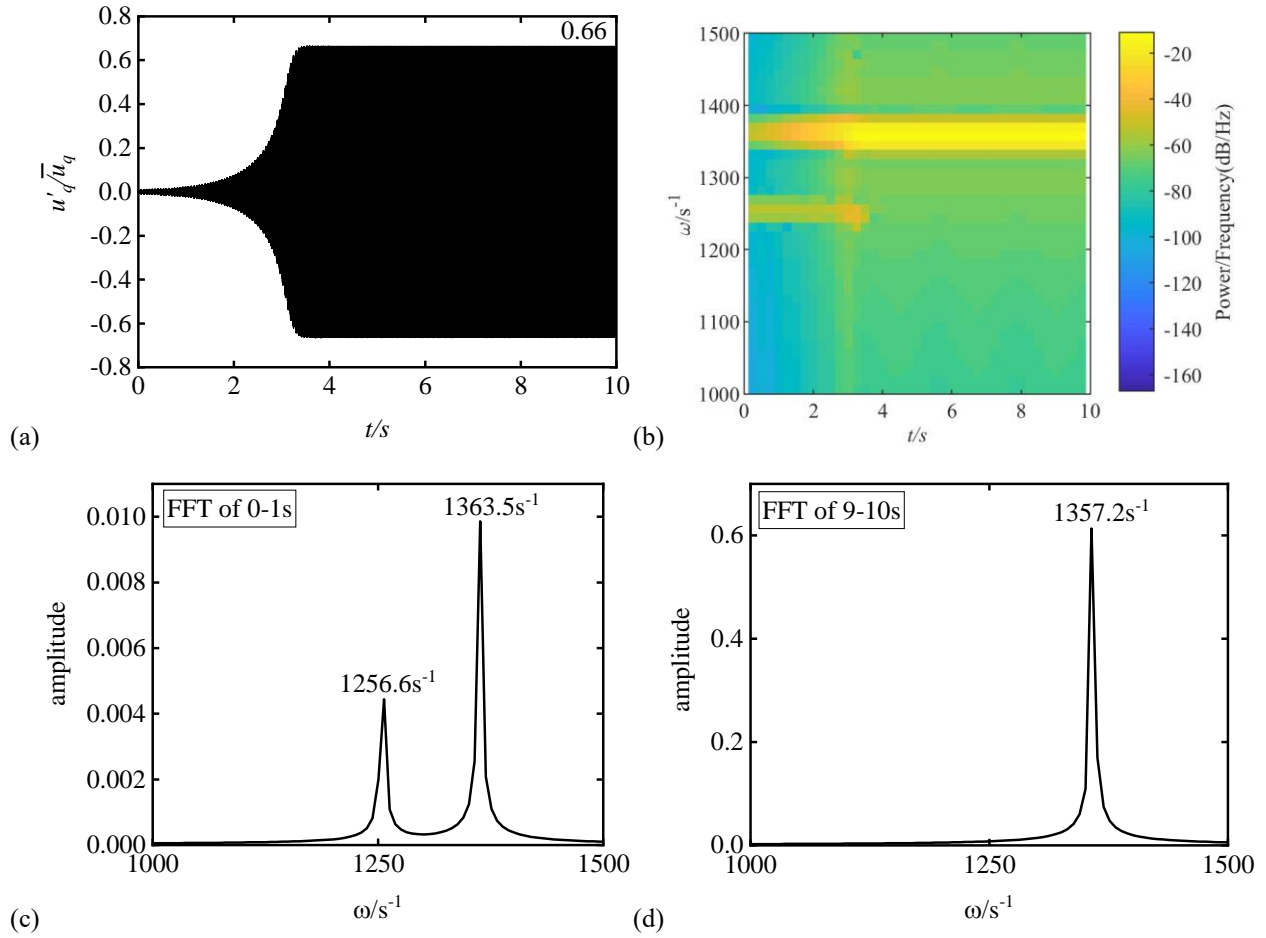
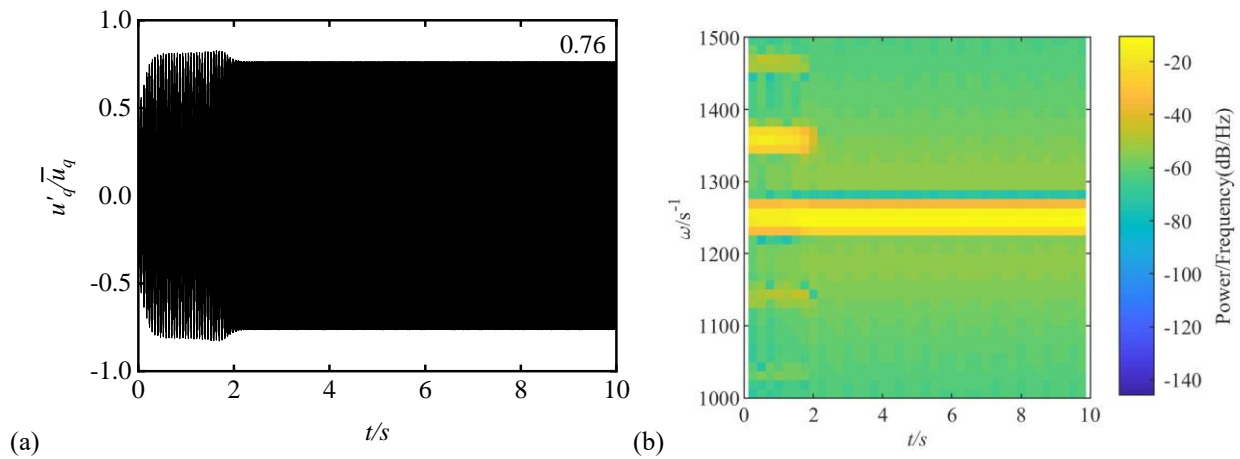


Fig. 3. (a) Time history of the acoustic velocity when the initial acoustic velocity is 0.01. (b) Spectrogram of the time history. (c) Spectrum of the time history for the time window [0-1s] of the time history. (d) Spectrum of the time history for the time window [9-10s] of the time history.



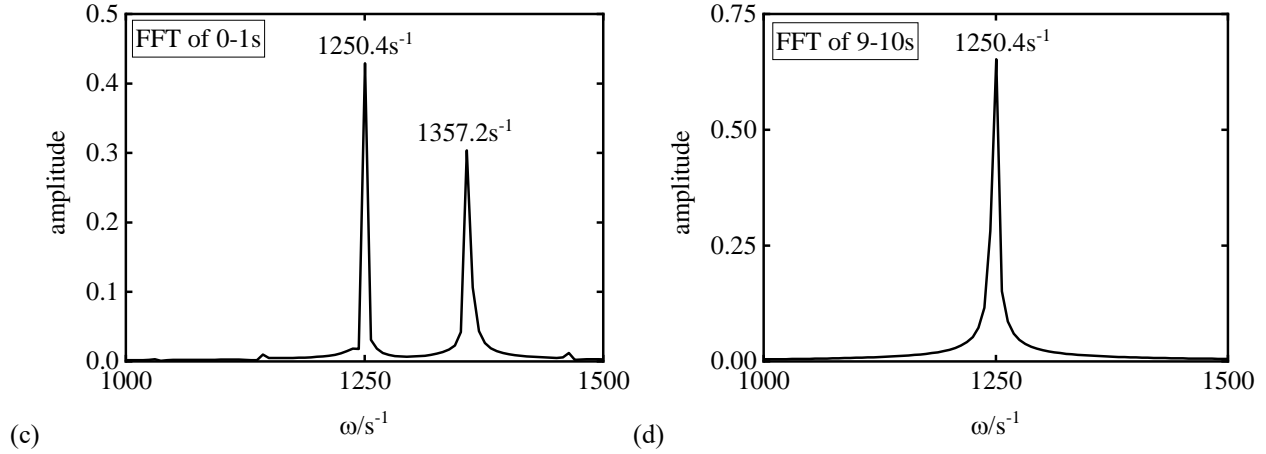


Fig. 4. (a) Time history of the acoustic velocity when the initial acoustic velocity is 0.5. (b) Spectrogram of the time history. (c) Spectrum of the time history for the time window [0-1s] of the time history. (d) Spectrum of the time history for the time window [9-10s] of the time history.

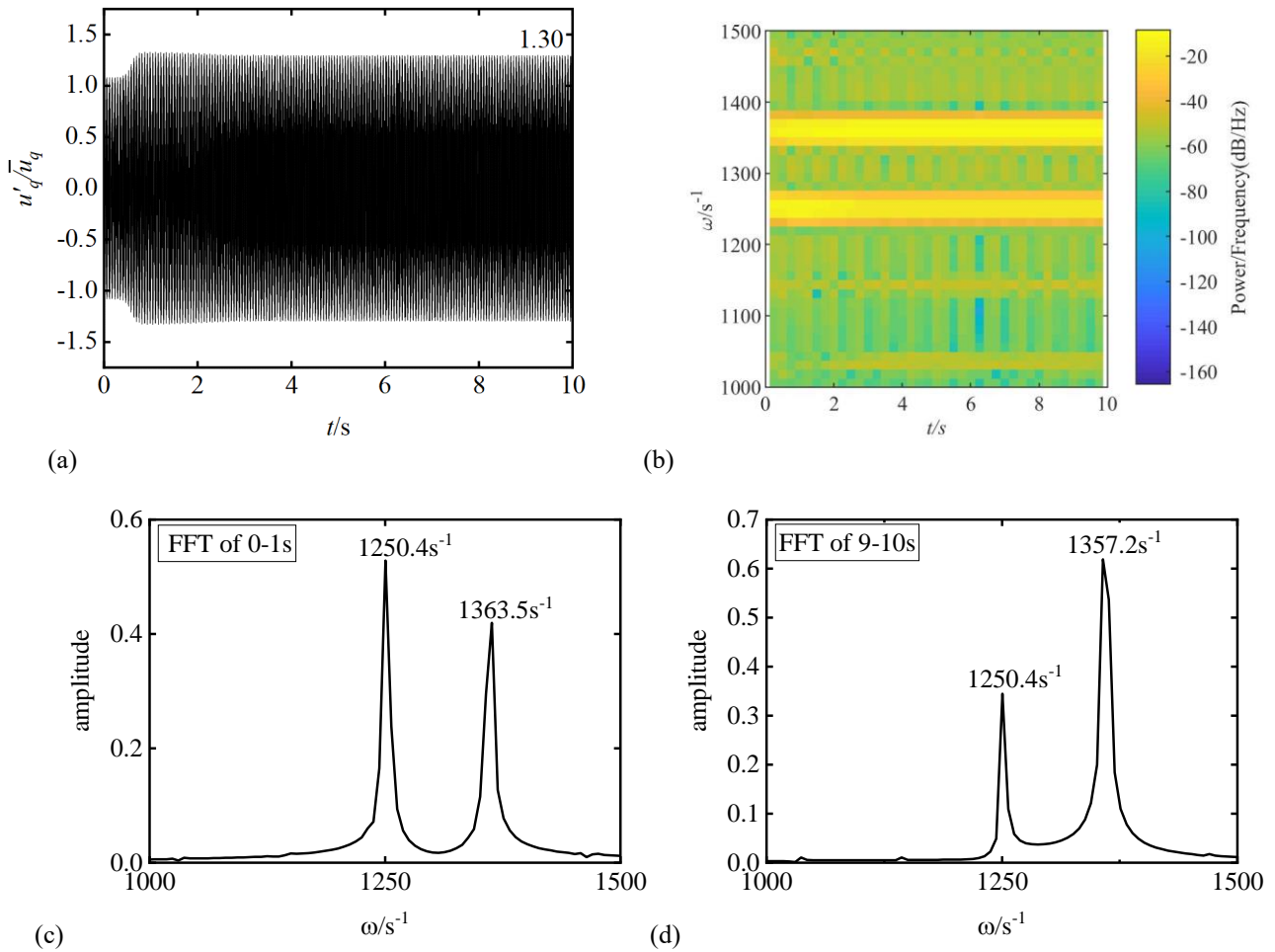


Fig. 5. (a) Time history of the acoustic velocity when the initial acoustic velocity is 1.1. (b) Spectrogram of the

time history. (c) Spectrum of the time history for the time window [0-1s] of the time history. (d) Spectrum of the time history for the time window [9-10s] of the time history.

When the initial acoustic velocity is set to 0.01, the oscillation is unstable: the acoustic velocity grows until a limit cycle with an amplitude of 0.66 is reached (see Fig. 3a). Fig. 3b shows the frequency content of this time history. This is shown in more detail in Figs. 3c and 3d. A Fast Fourier Transform (FFT) was performed for two time windows: one during [0-1s], early in the time history (see Fig. 3c), and another one during [9-10s], at the end of the time history (see Fig. 3d). It can be observed that initially there are two peaks in the spectrum, representing the two modes. However, during the limit cycle stage, only mode (1,0,1) prevails, while mode (1,0,0) disappears.

In Fig. 4, the initial acoustic velocity is set to 0.5. The oscillation is unstable and the acoustic velocity quickly reaches a limit cycle with amplitude 0.76. However, this time mode (1,0,1) disappears, and mode (1,0,0) becomes the dominant mode, which is the opposite of the case where the initial velocity is 0.01. A case, where both modes (1,0,0) and (1,0,1) are unstable and coexist throughout the entire time history, is shown in Fig. 5; here the initial velocity is set to 1.1.

As Figs. 3, 4 and 5 illustrate, the limit cycle amplitude depends on the initial condition. This dependence is shown quantitatively in Fig. 6.

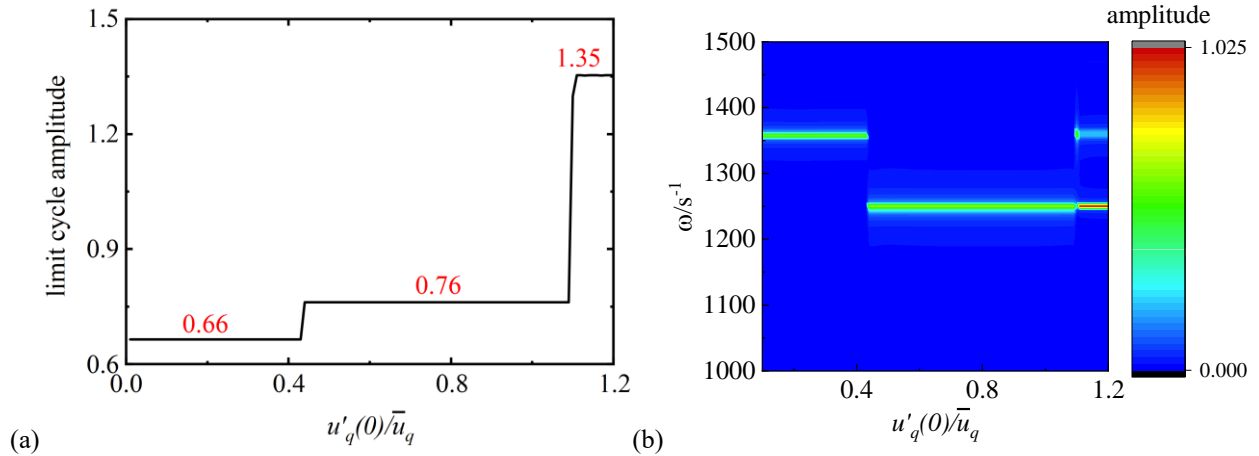


Fig. 6. (a) Amplitude of the limit cycle for different initial acoustic velocities. (b) Frequency content of the limit cycle for different initial acoustic velocities.

Fig. 6a gives the limit cycle amplitude as a function of the initial velocity. The corresponding frequency distribution in Fig. 6b (obtained by FFT over the [9-10s] time window of different initial acoustic velocities), shows

the emergence of the dominant mode: when the initial acoustic velocity is between 0.01 and 0.44, the limit cycle amplitude is 0.66 and mode (1,0,1) is dominant; when the initial acoustic velocity is between 0.44 and 1.09, the limit cycle amplitude is 0.76 and mode (1,0,0) is dominant. When the initial acoustic velocity is beyond 1.1, the limit cycle amplitude is 1.35 and the two modes coexist. The jumps in limit cycle amplitude and frequency at the initial velocities 0.44 and 1.09 visible in Fig. 6a bear no resemblance to the results for the complex eigenfrequencies; these would suggest jumps at initial amplitudes of 0.76 (see Fig. 2b). Therefore, in situations where two modes coexist, the complex eigenfrequency method fails to predict the system behavior correctly. This conclusion is consistent with the findings of Bigongiari and Heckl [62].

In practical combustion systems, the acoustic velocity amplitude is smaller than the mean flow velocity. Therefore, the following analysis is limited to cases where the initial velocities are 0.01 and 0.5 times the mean velocity.

3.2.1 Analysis to determine which mode will dominate

Again, we consider only the two modes (1,0,0) and (1,0,1), and label them mode 1 and mode 2, respectively. Then the sum in the integral governing Eq. (19) can be truncated to include only two terms. These two terms are spelled out explicitly to give

$$\begin{aligned}
 u_q'(t) = & \underbrace{-\frac{\gamma-1}{c_0^2} \int_0^t G_1 \left[\frac{e^{j\omega_1(t-t')}}{2} - \frac{e^{-j\omega_1(t-t')}}{2} \right] \cdot q'(t') dt'}_{u_{q1}'} + \frac{\phi_0}{c^2} j\omega_1 G_1 \cos(\omega_1 t) \\
 & \underbrace{-\frac{\gamma-1}{c_0^2} \int_0^t G_2 \left[\frac{e^{j\omega_2(t-t')}}{2} - \frac{e^{-j\omega_2(t-t')}}{2} \right] \cdot q'(t') dt'}_{u_{q2}'} + \frac{\phi_0}{c^2} j\omega_2 G_2 \cos(\omega_2 t).
 \end{aligned} \tag{27}$$

The term labelled u_{q1}' in Eq. (27) only contains the parameters ω_1 , G_1 , which relate to mode (1,0,0), while the term labelled u_{q2}' only contains ω_2 , G_2 and relates to mode (1,0,1). The time histories of u_{q1}' and u_{q2}' can therefore be used to analyze the coupling mechanism between these modes. At the same time, the time history of the acoustic velocity is given for the case where there is only one mode in the system with the same initial acoustic velocity as for the bimodal case.

Results are shown in Fig. 7 for an initial velocity amplitude of 0.01, and in Fig. 8 for an initial amplitude of 0.5. Parts (a) of Figs. 7 and 8 show the time histories for each of the two modes in isolation: at the top is the time history of mode (1,0,0); at the bottom is that of mode (1,0,1). In parts (b) of these figures, both modes are present, and the

time histories of u'_{q1} and u'_{q2} are shown. Parts (c) and (d) of these figures show how the frequency spectra of u'_{q1} and u'_{q2} change over time.

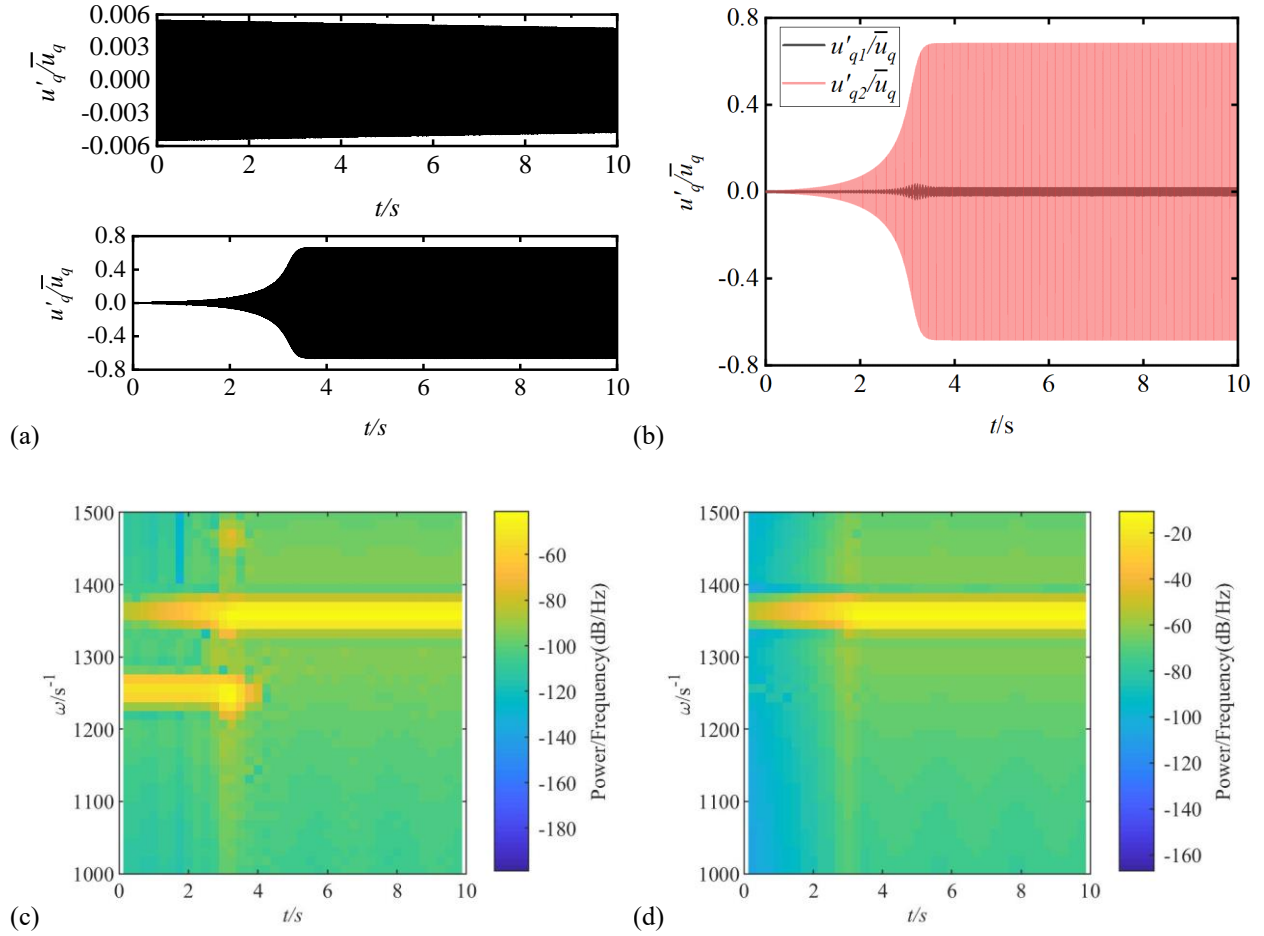


Fig. 7. Results for the case where the initial acoustic velocity is 0.01. (a) Time history of the acoustic velocity when there is only one mode in the system with the same initial acoustic velocity as for the bimodal case. Top: mode (1,0,0), below: mode (1,0,1); (b) acoustic velocities u'_{q1} and u'_{q2} given by Eq. (27); (c) spectrogram of u'_{q1} ; (d) spectrogram of u'_{q2} .

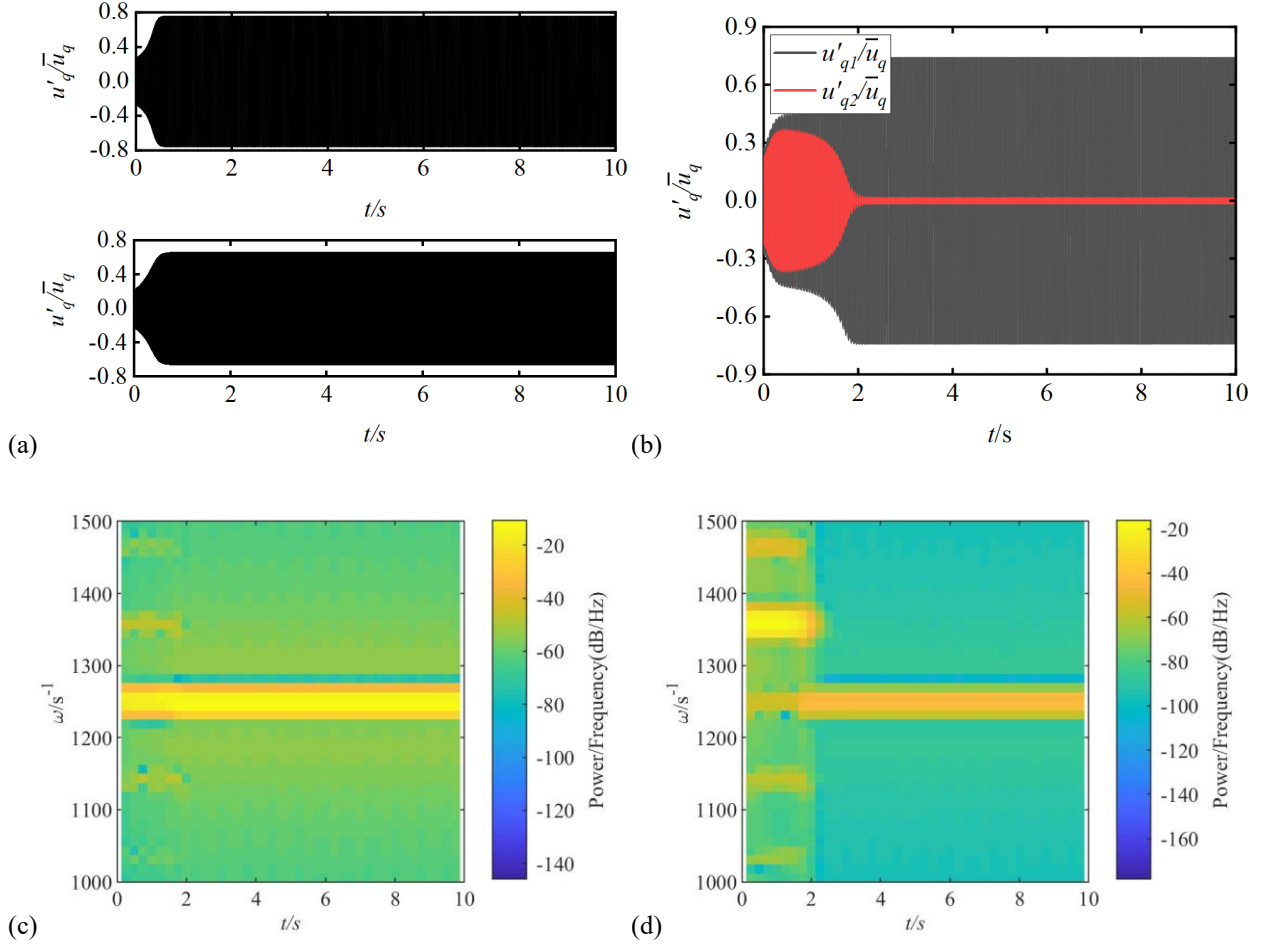


Fig. 8. Results for the case where the initial acoustic velocity is 0.5. (a) Time history of the acoustic velocity when there is only one mode in the system with the same initial acoustic velocity as for the bimodal case. Top: mode (1,0,0), below: mode (1,0,1); (b) acoustic velocities u'_{q1} and u'_{q2} given by Eq. (27); (c) spectrogram of u'_{q1} ; (d) spectrogram of u'_{q2} .

Fig. 7b illustrates the behaviour of u'_{q1} and u'_{q2} . u'_{q1} increases slightly and then stabilizes in a limit cycle with a very small amplitude. u'_{q2} initially grows exponentially, then the growth slows down until a limit cycle with a considerable amplitude is reached. The spectrograms in Figs. 7c and 7d shed light on how the frequency content of the two time histories evolves with time. u'_{q1} (see Fig. 7c) starts with the frequency of around 1250 s^{-1} , which is that of mode (1,0,0), but this frequency disappears from the spectrum after about 4s; in the mean time, mode (1,0,1) (recognizable by the yellow band around 1360 s^{-1}) emerges and persists until the end of the time history. It is evident that during the time history a transition is going on from mode (1,0,0) to mode (1,0,1). This transition is a

manifestation of the *nonlinear coupling* between the two modes; it cannot occur for a superposition of different modes in a linear situation. u'_{q_2} (see Fig. 7d) exclusively contains frequencies around the value 1360 s^{-1} , which is associated with mode (1,0,1).

Fig. 8 shows another example of mode transition, this time from mode (1,0,1) to mode (1,0,0). In isolation, each mode is unstable and reaches a limit cycle (with amplitude 0.76 for mode (1,0,0) and 0.66 for mode (1,0,1)), as can be seen from Fig. 8a. Fig. 8b shows the time histories of u'_{q_1} and u'_{q_2} , with both modes included in the analysis. Mode (1,0,0) persists throughout, while the amplitude of mode (1,0,1) decreases and approaches zero after about 2 s. Fig. 8c illustrates the dominance of mode (1,0,0). Fig. 8d provides evidence of the transition in frequency, from mode (1,0,1) to mode (1,0,0).

Our predictions indicate that the nonlinear interaction between modes has a mutually inhibitory effect, i.e. one mode tries to push out the other mode. This is significant for the development of control strategies to mitigate thermoacoustic instabilities. Not all unstable modes need to be suppressed; an unstable mode with a large limit cycle might get pushed out by a mode with a smaller limit cycle amplitude, and this would be beneficial for the combustion system.

3.2.2 Phase analysis

Thermoacoustic instabilities originate from the coupling between unsteady heat release and acoustic pressure. Rayleigh was the first to explain the coupling mechanism and formulated a stability criterion in terms of the Rayleigh index defined by [66]

$$Gain = \int_0^T q'(t) p'(t) dt. \quad (28)$$

$p'(t)$ is the acoustic pressure, and $q'(t)$ is the unsteady part of the heat release rate. This Rayleigh index is a measure of the energy gained by the thermoacoustic coupling. In our model, there are no acoustic loss mechanisms: the inlet and outlet boundaries are assumed to be perfectly rigid, so no acoustic energy is radiated from the cylinder ends; also, we assume that there is no dissipation due to friction or heat transfer. It is therefore possible to deduce the stability behaviour simply from the sign of the Rayleigh index: if $Gain > 0$, the acoustic field gains energy from the unsteady heat release rate and the system is unstable; if $Gain < 0$, the acoustic field loses energy and the system is stable.

Eq. (28) can be expressed in the frequency domain by

$$Gain = 2 \int_0^{\infty} |S_{pq}(f)| \cos \phi_{pq}(f) df, \quad (29)$$

where $S_{pq}(f)$ are the Fourier coefficients of the cross-spectrum of $p'(t)$ and $q'(t)$, and $\phi_{pq}(f)$ are the relative phase angles. If only the two modes (1,0,0) and (1,0,1) are present, Eq. (29) can be simplified as follows:

$$Gain = 2 \left(|S_{pq}(\text{Re}(\Omega_{100}))| \cos \phi_{pq}(\text{Re}(\Omega_{100})) + |S_{pq}(\text{Re}(\Omega_{101}))| \cos \phi_{pq}(\text{Re}(\Omega_{101})) \right), \quad (30)$$

where the first and second terms on the right-hand side of Eq. (30) denote the energy gained by mode (1,0,0) and mode (1,0,1), respectively. If the relative phase angle of mode (1,0,0), $\phi_{pq}(\text{Re}(\Omega_{100}))$, is between $-\pi/2$ and $\pi/2$ (modulus 2π), then that mode is unstable (unless there is dissipation of acoustic energy, which we do not consider in this paper). The same applies to mode (1,0,1). An expression for the pressure can be derived from Eq. (14) by using the relationship between pressure and velocity potential, which results from the momentum equation:

$$p'(\vec{r}, t) = -\bar{\rho} \frac{\partial \phi}{\partial t} = \bar{\rho} \frac{\gamma - 1}{2c^2} \sum_{mnk} \left\{ \begin{array}{l} e^{j\omega_{mnk}t} (j\omega_{mnk}) \int_0^t g_{mnk}(\vec{r}, \vec{r}') \Big|_{\vec{r}' = \vec{r}_q} e^{-j\omega_{mnk}t'} q'(t') dt' \\ + e^{j\omega_{mnk}t} g_{mnk}(\vec{r}, \vec{r}') \Big|_{\vec{r}' = \vec{r}_q} e^{-j\omega_{mnk}t} q'(t) \\ - e^{-j\omega_{mnk}t} (-j\omega_{mnk}) \int_0^t g_{mnk}(\vec{r}, \vec{r}') \Big|_{\vec{r}' = \vec{r}_q} e^{j\omega_{mnk}t'} q'(t') dt' \\ - e^{-j\omega_{mnk}t} g_{mnk}(\vec{r}, \vec{r}') \Big|_{\vec{r}' = \vec{r}_q} e^{j\omega_{mnk}t} q'(t) \end{array} \right\} + \bar{\rho} \frac{\phi_0}{c^2} \left(\frac{\partial^2 G}{\partial t' \partial t} \right) \Big|_{\substack{t'=0 \\ r'=\vec{r}_q}}. \quad (31)$$

This equation can be rewritten as explained in section 2.4.2 to give an expression for the acoustic pressure at the flame \vec{r}_q ,

$$p'(\vec{r}_q, t) = \bar{\rho} \frac{\gamma - 1}{c^2} \sum_{mnk} j\omega_{mnk} g_{mnk}(\vec{r}, \vec{r}') \Big|_{\substack{\vec{r}' = \vec{r}_q \\ \vec{r} = \vec{r}_q}} \left[e^{j\omega_{mnk}t} I_{mnk1}(t) + e^{-j\omega_{mnk}t} I_{mnk2}(t) \right] \\ + \bar{\rho} \frac{\phi_0}{c^2} \sum_{mnk} g_{mnk}(\vec{r}, \vec{r}') \Big|_{\substack{\vec{r}' = \vec{r}_q \\ \vec{r} = \vec{r}_q}} \cdot j\omega_{mnk}^2 \sin(\omega_{mnk}t). \quad (32)$$

The time history of the pressure can now be obtained with the numerical iteration method used earlier (see Section 2.4.2) to calculate $u'_q(t)$. With $u'_q(t)$ known, the time history of the unsteady heat release can be calculated from the time-domain version of Eq. (9). The relative phase angles of both modes are obtained from FFT

(with a choice of 1s for the time interval and 0.7s for the overlap).

The relative phase angles and the amplitudes of the two modes (1,0,0) and (1,0,1) are shown as functions of time in the two figures below; Fig. 9 is for a low initial velocity of 0.01, while Fig. 10 is for the higher initial velocity of 0.5. The black curves with squares in these figures are for mode (1,0,0), and the red curves with circles are for mode (1,0,1).

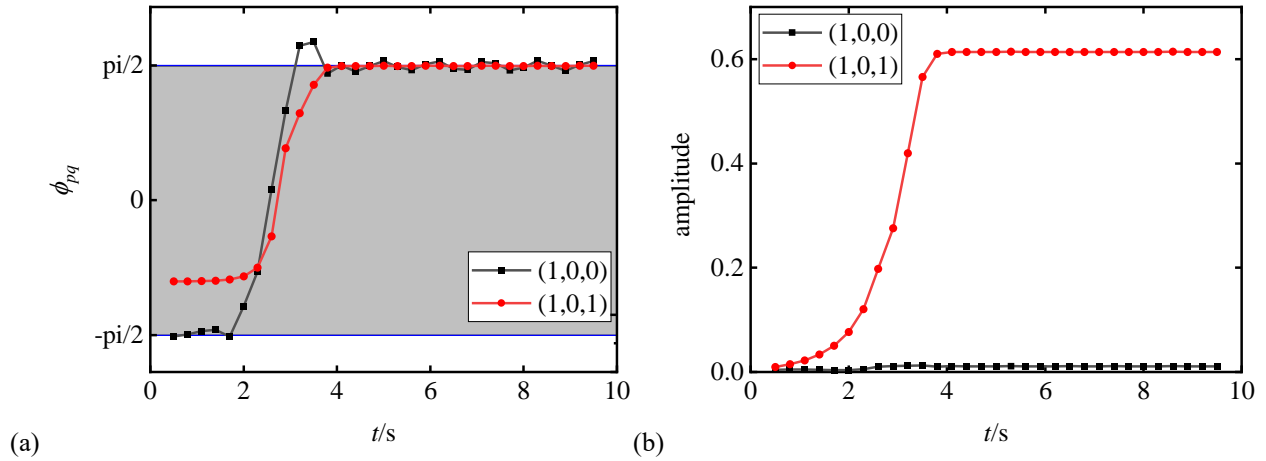


Fig. 9. Results displayed as functions of time t for the case where the initial acoustic velocity is 0.01. (a) Relative phase angles of both modes; the grey shading marks the phase range $-\pi/2$ to $\pi/2$, where the energy gain is positive; (b) amplitude of both modes.

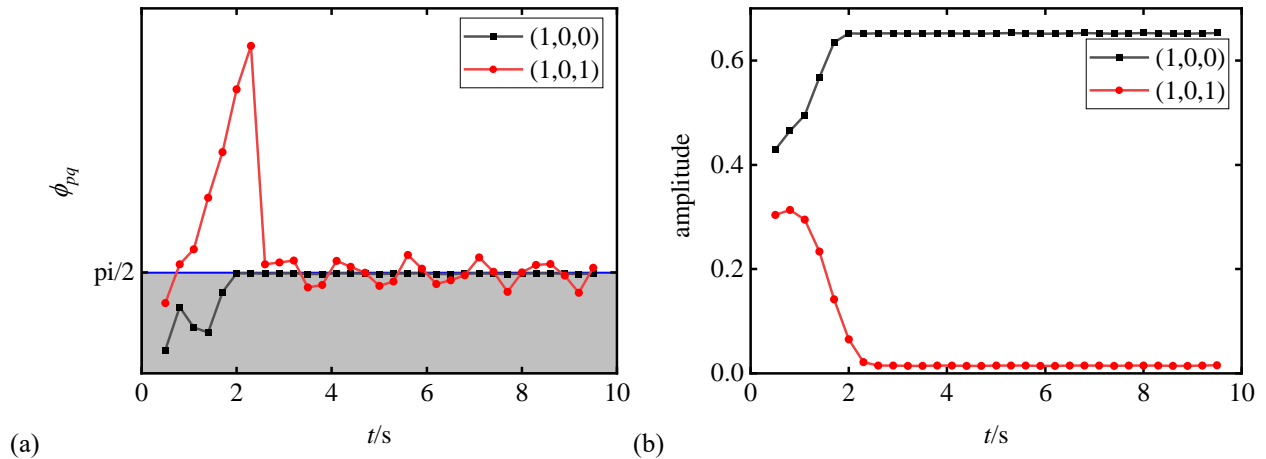


Fig. 10. Results displayed as functions of time t for the case where the initial acoustic velocity is 0.5. (a) Relative phase angles of both modes; the grey shading marks the phase range 0 to $\pi/2$, where the energy gain is positive; (b) amplitude of both modes.

We make the following observations from Fig. 9. Early on in its time history mode (1,0,0) has a phase angle that

hovers around $-\pi/2$, and the amplitude does not change. Subsequently, the relative phase angle grows rapidly, overshoots the value $\pi/2$, then comes back down to $\pi/2$, and oscillates around this value for the remaining time history. As this goes on, the amplitude exhibits a slight increase, then decreases to a very low value and remains at this level. The behaviour of mode (1,0,1) is different. The relative phase angle of this mode is between $-\pi/2$ and $\pi/2$ at the beginning of the time history; it increases steadily and eventually stabilizes at $\pi/2$, where it remains for the rest of the time history. At the same time, the amplitude of this mode increases steadily until it reaches the limit cycle, as shown in Fig. 9b. For both modes, the evolution of the amplitude is consistent with the findings of the phase analysis.

Fig. 10 shows equivalent results for an initial disturbance of 0.5. The relative phase angle of mode (1,0,0) remains within the range of $[-\pi/2, \pi/2]$ throughout, stabilizing finally on $\pi/2$. This results in a rapid increase in the amplitude until the limit cycle is reached. Mode (1,0,1) exhibits a very different behaviour. The relative phase angle initially falls within the range of $[-\pi/2, \pi/2]$, but grows rapidly and exceeds the value $\pi/2$ significantly before decreasing back to $\pi/2$ and then hovering around this value. As a consequence, the amplitude experiences a slight increase, followed by a continuous decrease, and soon disappears completely. Again, the evolution of the amplitude is consistent with the findings of the phase analysis for both modes.

The two cases displayed in Figs. 9 and 10 show that initially both modes gain energy, but only one of the modes appears in the limit cycle that forms as time progresses. We conclude from this that there is an inhibitory effect among the modes, and that the relative phase angle is the key quantity that determines which mode pushes out the other mode. Phase analysis has served here as a powerful tool to explain the evolution of the two modes. We therefore use it again in the next section to explain the phenomenon of mode switch.

3.3 Mode switch

In practical combustion systems, the dominant mode that governs system instability can change with variations in the operating conditions, a phenomenon referred to as "mode switch". In order to investigate the underlying mechanism of mode switch, we will use the time history method again, combined with phase analysis. We will simulate changes in the operating conditions by changes in the FDF given in Eq. (8). The key parameters are the interaction indices and the delay time; they depend on the coefficients τ_0, τ_1, g_0, g_1 in Eq. (10). By changing g_0 (or g_1), we can vary the interaction indices; by changing τ_0 (or τ_1), we can vary the delay time.

3.3.1 Influence of changes in the interaction indices

The interaction indices represent the coupling intensity between the unsteady heat release and acoustic pressure. In order to investigate their influence, we change the value of g_0 abruptly during the calculation of the time history, and then analyse the time histories before and after the abrupt change. Fig. 11 shows four examples.

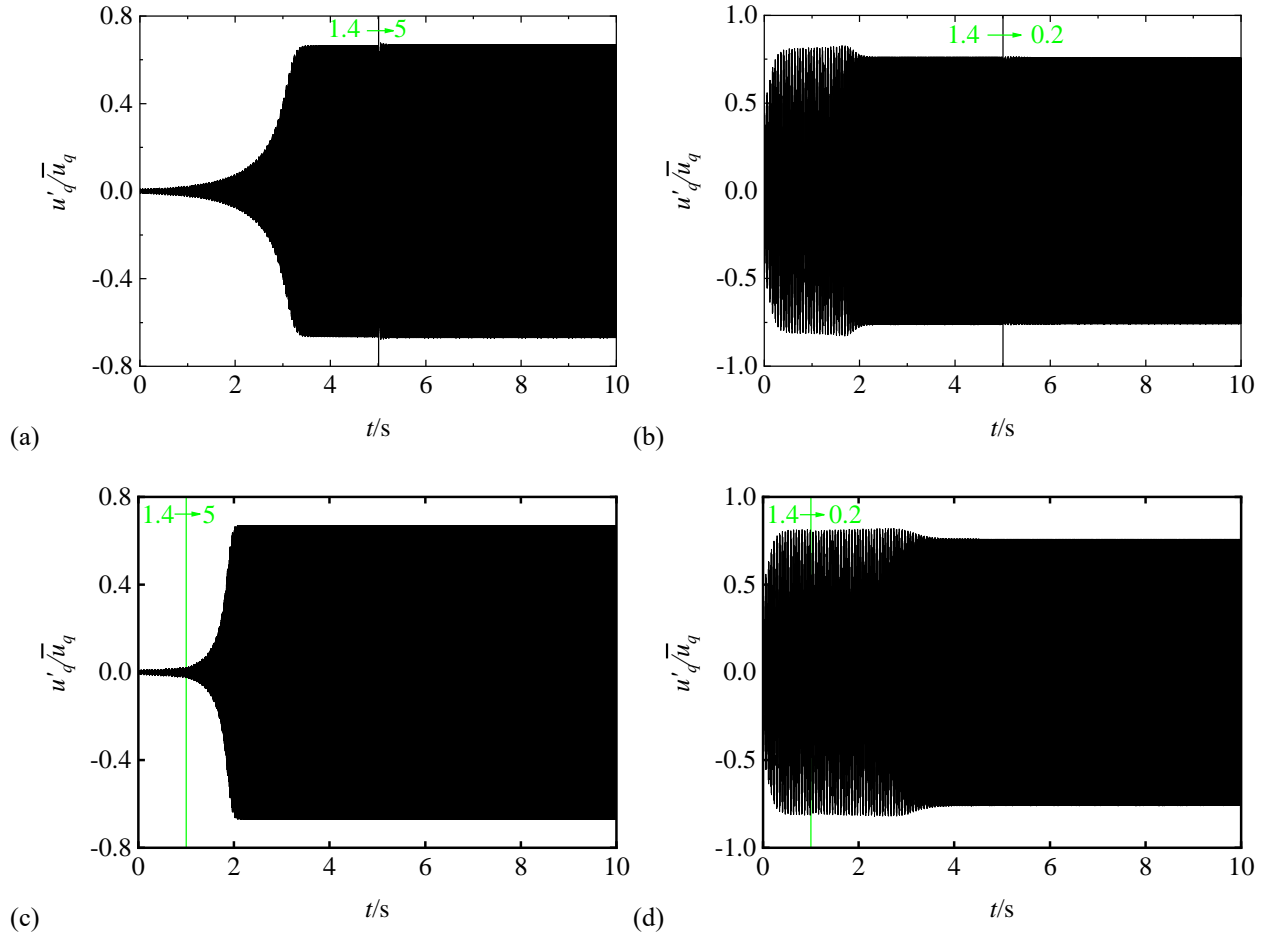


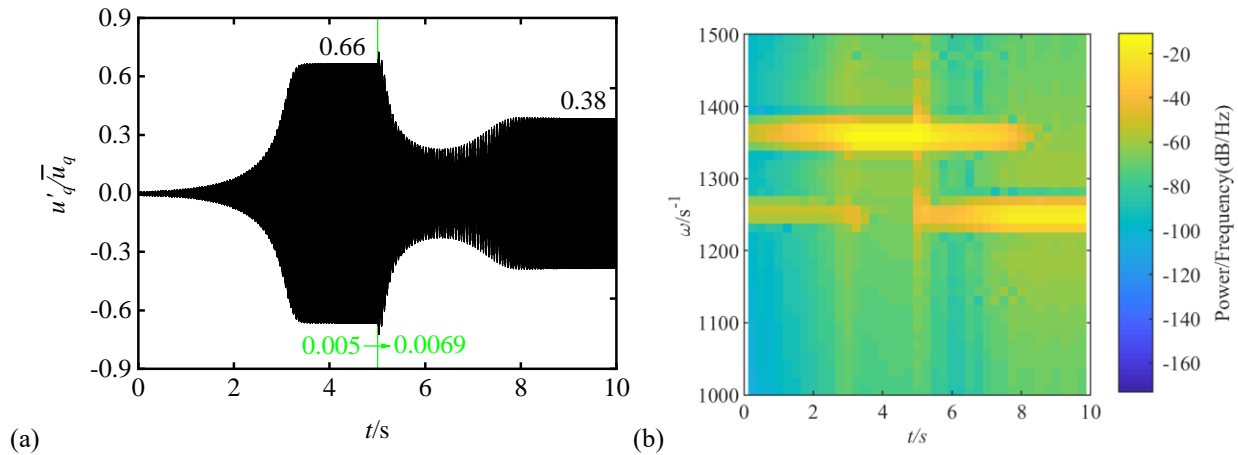
Fig. 11. Time history of the acoustic velocity when g_0 is abruptly changed, while the other parameters in the heat release expression remain constant ($g_1 = 0.3$, $\tau_0 = 5 \times 10^{-3}$ s, $\tau_1 = 4.4 \times 10^{-3}$ s). The vertical greenline marks the time of the change. (a) The initial acoustic velocity is 0.01; g_0 is increased from 1.4 to 5 at $t = 5$ s. (b) The initial acoustic velocity is 0.5; g_0 is decreased from 1.4 to 0.2 at $t = 5$ s. (c) The initial acoustic velocity is 0.01; g_0 is increased from 1.4 to 5 at $t = 1$ s. (d) The initial acoustic velocity is 0.5; g_0 is decreased from 1.4 to 0.2 at $t = 1$ s.

In Figs. 11a (low initial velocity amplitude, g_0 increases) and 11b (high initial velocity amplitude, g_0 decreases), the change occurs at time $t=5$ s, when the limit cycle is fully established. In both cases, the acoustic velocity experiences a minor amplitude change and quickly returns to its original limit cycle. In Figs. 11c and 11d, the change in g_0 occurs at the earlier time $t=1$ s, i.e., during the transient phase before the limit cycle has evolved. Comparison of Figs. 11a and 11c shows that the time to reach the limit cycle is considerably shortened by the sudden increase in g_0 . A sudden decrease in g_0 delays the evolution of the limit cycle, as can be seen by comparing Figs. 11b and 11d.

Therefore, we can draw the conclusion that altering g_0 does not affect the limit cycle amplitude or the dominant mode, but rather influences the time required to reach the limit cycle. This is because the interaction indices only affect the *magnitude*, but not the sign of the energy gain. Therefore they have no effect on the limit cycle itself, but they do significantly affect the time it takes to reach the limit cycle. This observation is consistent with the energy analysis presented in Eq. (29). The changes in the interaction indices alter the coupling intensity $S_{pq}(f)$ between the modes, but *not* the relative phase angles $\phi_{pq}(f)$.

3.3.2 Influence of changes in the delay time

The delay time τ has a strong influence on the relative phase angle $\phi_{pq}(f)$, so a change in τ can lead to a change in the *sign* of the energy gain. This will have a profound effect on the stability behaviour and limit cycle amplitudes. In order to investigate the effect of changing the delay time, we increase the value of τ_0 abruptly at time $t = 5$ s from 0.005 s to 0.0069 s. The resulting time history is shown in Fig. 12a, and its frequency content is displayed in Figs. 12b, c, d.



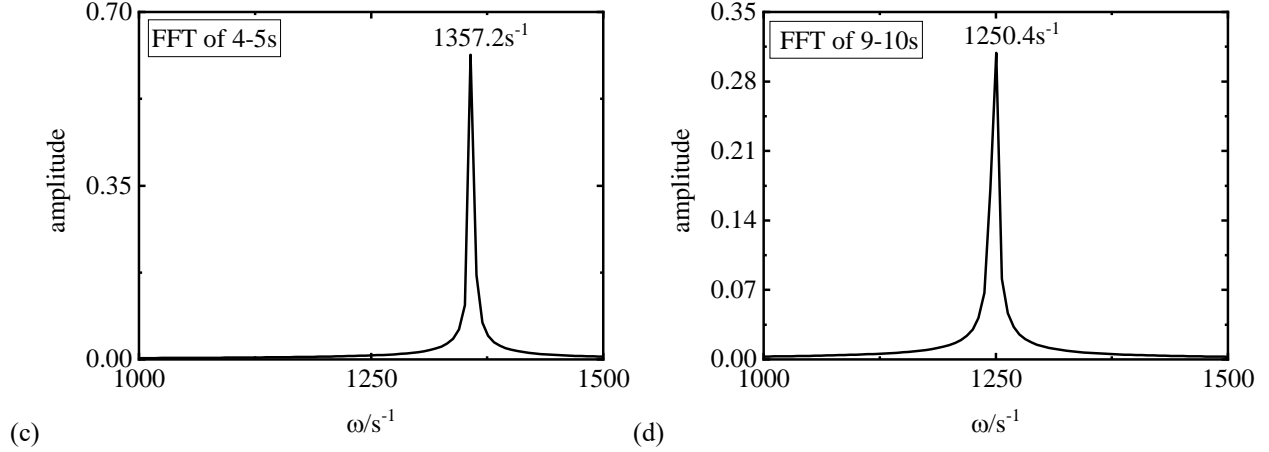


Fig. 12. (a) Time history of the acoustic velocity when τ_0 is abruptly changed, while the other parameters in the heat release expression remain constant ($g_0 = 1.4$, $g_1 = 0.3$, $\tau_1 = 4.4 \times 10^{-3}$ s); the change of τ_0 is from 0.005 s to 0.0069 s and occurs at time $t = 5$ s; this is marked by a green vertical line; the initial acoustic velocity is 0.01. (b) Spectrogram showing the evolution of the time history in part (a). (c) FFT of time window [4-5s] of the time history in part (a). (d) FFT of time window [9-10s] of the time history in part (a).

We observe that before the change of τ_0 , the system is initially unstable and then reaches the limit cycle with an amplitude of 0.66 (consistent with Fig. 3a). After the change, the acoustic velocity experiences a rapid amplitude decrease, which lasts for a short time interval; subsequently, the oscillation evolves into a new limit cycle with a lower amplitude of 0.38. The spectrogram in Fig. 12b shows the evolution of the two modes that form the time history in Fig. 12a. In the initial 5 s, i.e. before the jump in τ_0 , the amplitude of mode (1,0,0) (about 1250 Hz) gradually decreases until it nearly disappears, while the amplitude of mode (1,0,1) (about 1360 Hz) increases until a limit cycle is reached. In the subsequent 5 s, i.e. after the jump in τ_0 , the situation reverses completely: the amplitude of mode (1,0,0) gradually increases from a small value until a new limit cycle is reached, while the amplitude of mode (1,0,1) decreases gradually until it nearly disappears. Accurate values for the modal frequencies can be ascertained from the spectra in Figs. 12c and 12d, which were calculated by FFT for two different time windows. In Fig. 12c, the time window is [4-5s], which is just before the jump in τ_0 ; in Fig. 12d, the time window is [9-10s], which is well after the jump. It is evident that the dominant mode switches from mode (1,0,1) to mode (1,0,0) following the change in τ_0 .

Further insight into the mode-switch phenomenon can be gained by plotting the relative phase angles and amplitudes of both modes over the full time interval [0-10s]. These plots are shown in Fig. 13; they were calculated

by applying FFT and phase analysis to the time history in Fig. 12a.

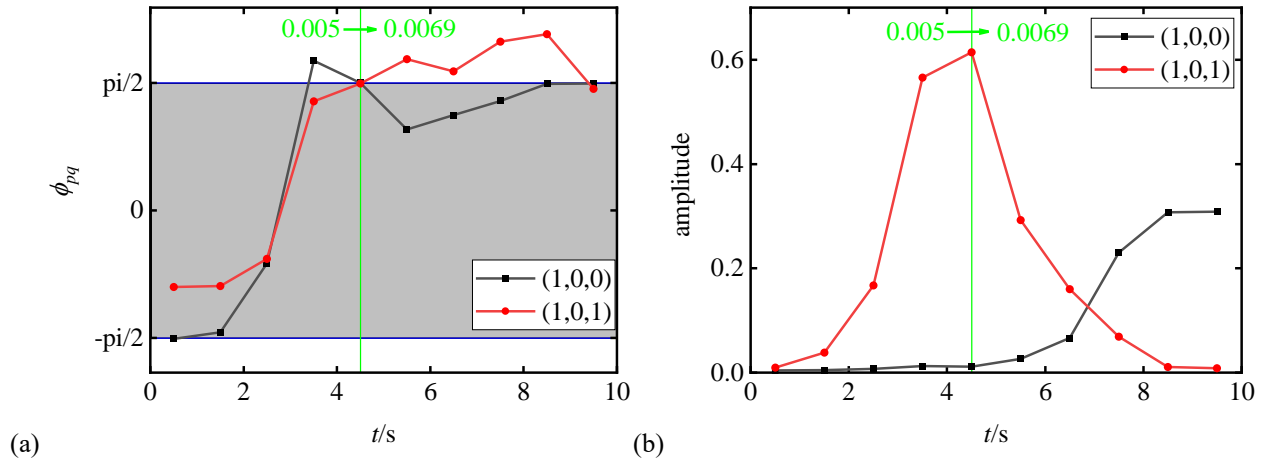


Fig. 13. Evolution of the two modes forming the time history in Fig. 12a. (a) Relative phase angles of modes (1,0,0) and (1,0,1); (b) acoustic velocity amplitude of modes (1,0,0) and (1,0,1). Grey shading marks the phase range $[-\pi/2, \pi/2]$, where the energy gain is positive. The time of the jump in τ_0 is marked by a green vertical line.

Both parts of the figure show that the mode switch becomes evident after the jump in τ_0 at $t = 5$ s. For mode (1,0,0) (black curve in Fig. 13), the phase ϕ_{pq} is in the grey region, which indicates positive energy gain, and consequently, the amplitude grows until about $t = 8$ s. After that, both phase and amplitude remain constant, at $\pi/2$ and approximately 0.3, respectively; at that stage, mode (1,0,0) has reached a limit cycle. Mode (1,0,1) (red curve in Fig. 13), on the other hand, loses energy after the jump in τ_0 : its phase is a little greater than $\pi/2$, and its amplitude decays continuously; this explains the gradual decrease and subsequent disappearance of mode (1,0,1).

From the above analysis, we can conclude that the key parameter for the mode switch is the delay time between the heat release rate and the acoustic field. This delay time determines the sign of the Rayleigh index, which is a measure for the energy gained by the acoustic field from the flame. The relative phase angle ϕ_{pq} of the individual modes also depends on this delay time. The phenomenon of mode switch is likely to occur when one of the phase angles crosses the thresholds $\pi/2$ or $-\pi/2$.

4. Conclusion

A Green's function approach was developed to investigate multimodal interaction in cylindrical combustion

systems, such as afterburners. An integral governing equation was derived for the acoustic velocity at the flame (which was modeled by an analytical FDF). The flame was modeled as a point source with a heat release rate given by a nonlinear time-lag law. Two methods were presented to solve the integral equation: a method based on the Laplace transform, which gives an algebraic equation for the complex eigenfrequency, and a numerical iteration method, which solves the integral equation directly and hence yields the time history of the acoustic velocity at the flame. The calculation of the complex eigenfrequencies gave reliable results for a single mode, but failed to capture the nonlinear interaction between modes. In contrast, the calculation of the time history provided reliable results across-the-board and shed light on the evolution of individual modes coexisting in the combustion chamber.

We focused on the two modes (1,0,0) and (1,0,1) and calculated the time history of the total acoustic velocity. Different scenarios were observed, depending on the initial conditions. Both modes might coexist early in the time history, but later on, one of the modes would become dominant, forms a limit cycle and squeezes out the other mode. Coexistence of both modes was also observed. In general, the nonlinear interaction between the modes has a mutually inhibitory effect. This insight provides valuable guidelines for developing control strategies for thermoacoustic instabilities: not all unstable modes in a combustion system need to be suppressed; modes with a low limit cycle amplitude may be tolerable.

Further understanding was gained from our "phase analysis", which indicates whether an individual mode gains or loses energy during the thermoacoustic oscillation. We used this method to analyse the phenomenon of mode switch, which can occur in a combustion system when the operating conditions change. In order to simulate changing operating conditions, the interaction indices and delay times in the FDF were changed abruptly during the calculation of the time history. Phase analysis revealed that a sudden change in the interaction indices will have an impact on the time required to reach the limit cycle but not on the *amplitude* of the limit cycle. A dramatic change in the stability behaviour and limit cycle amplitude of the individual modes was observed when the delay time changed abruptly, and again this was explained by phase analysis. We conclude that the delay time plays a crucial role in the phenomenon of mode switch.

Acknowledgement

The research was supported by the Science Center for Gas Turbine Project of China (No. P2022-B-II-013-001)

and the National Natural Science Foundation of China (No. 52106038).

Appendix A. The derivation of expression of Green's function for the simplified geometry

The governing equation of Green's function is

$$\frac{1}{c_0^2} \frac{\partial^2 G}{\partial t^2} - \nabla^2 G = \delta(\vec{r} - \vec{r}') \delta(t - t'). \quad (\text{A.1})$$

The definition of the Fourier transform is

$$\hat{G} = \int_{-\infty}^{+\infty} G e^{j\omega(t-t')} dt, \quad (\text{A.2})$$

$$G = \frac{1}{2\pi} \int_{-\infty}^{+\infty} \hat{G} e^{j\omega(t-t')} d\omega. \quad (\text{A.3})$$

Therefore,

$$F(\nabla^2 G) = \nabla^2 \hat{G}, \quad F\left(\frac{\partial G}{\partial t}\right) = j\omega \hat{G}, \quad F\left(\frac{\partial^2 G}{\partial t^2}\right) = -\omega^2 \hat{G}. \quad (\text{A.4})$$

where F denotes the Fourier transform operator. Application of the Fourier transform to Eq. (A.1) yields

$$\nabla^2 \hat{G} - \frac{1}{c_0^2} (-\omega^2) \hat{G} = -\delta(\vec{r} - \vec{r}'). \quad (\text{A.5})$$

With $k_0 = \frac{\omega}{c_0}$, we can write

$$\nabla^2 \hat{G} + k_0^2 \hat{G} = -\delta(\vec{r} - \vec{r}'). \quad (\text{A.6})$$

\hat{G} can be represented by a sum of eigenfunctions ψ_i ,

$$\hat{G} = \sum_i A_i \psi_i(\vec{r}). \quad (\text{A.7})$$

Substitution of Eq. (A.7) into Eq. (A.6) yields

$$\sum_i A_i \nabla^2 \psi_i(\vec{r}) + k_0^2 \sum_i A_i \psi_i(\vec{r}) = -\delta(\vec{r} - \vec{r}'). \quad (\text{A.8})$$

The eigenfunctions ψ_i , are the solutions of the three-dimensional Helmholtz equation

$$\nabla^2 \psi_i(\vec{r}) + k_i^2 \psi_i(\vec{r}) = 0. \quad (\text{A.9})$$

If Eqs. (A.8) and (A.9) are combined, the following equation is obtained,

$$\sum_i (k_0^2 - k_i^2) A_i \psi_i(\vec{r}) = -\delta(\vec{r} - \vec{r}'). \quad (\text{A.10})$$

Multiplication of Eq. (A.10) by $\psi_j^*(\vec{r})$, which is the complex conjugate of $\psi_j(\vec{r})$, leads to

$$\psi_j^*(\vec{r}) \sum_i (k_0^2 - k_i^2) A_i \psi_i(\vec{r}) = -\psi_j^*(\vec{r}) \delta(\vec{r} - \vec{r}'). \quad (\text{A.11})$$

This is integrated over the volume v of the cylindrical tube, and the orthogonality of the eigenfunctions,

$$\int \psi_i \psi_j^* dv = \Gamma_j \delta_{ij}, \quad (\text{A.12})$$

(where Γ_j is a positive number) is then exploited to give

$$(k_0^2 - k_j^2) A_j \Gamma_j = -\psi_j^*(\vec{r}'). \quad (\text{A.13})$$

This can be solved for A_j to give

$$A_j = \frac{-\psi_j^*(\vec{r}')}{(k_0^2 - k_j^2) \Gamma_j}. \quad (\text{A.14})$$

Substitution into Eq. (A.7) then leads to

$$\hat{G} = \sum_i \frac{-\psi_i(\vec{r}) \psi_i^*(\vec{r}')}{(k_0^2 - k_i^2) \Gamma_i}. \quad (\text{A.15})$$

We solve the Helmholtz equation with a separation of variables approach by putting $\psi_i(\vec{r}) = \phi_i(r, \varphi) f_i(z)$

$$\left(\frac{\partial^2}{\partial r^2} + \frac{1}{r^2} \frac{\partial^2}{\partial \varphi^2} + \frac{1}{r} \frac{\partial}{\partial r} \right) \phi_i(r, \varphi) f_i(z) + \phi_i(r, \varphi) \frac{\partial^2 f_i(z)}{\partial z^2} + k_i^2 \phi_i(r, \varphi) f_i(z) = 0. \quad (\text{A.16})$$

Both sides of this equation are divided by $\psi_i(\vec{r}) = \phi_i(r, \varphi) f_i(z)$ to give

$$\frac{\nabla^2 \phi_i(r, \varphi)}{\phi_i(r, \varphi)} + \frac{\partial^2 f_i(z)}{\partial z^2} \frac{1}{f_i(z)} + k_i^2 = 0. \quad (\text{A.17})$$

Assuming that the z -dependent part of this equation is independent of r and φ , and therefore has to be a constant, we get

$$\frac{\partial^2 f_i(z)}{\partial z^2} \frac{1}{f_i(z)} = -k_z^2, \quad (\text{A.18})$$

or

$$\frac{d^2 f_i(z)}{dz^2} + k_z^2 f_i(z) = 0, \quad (\text{A.19})$$

which has the following solution,

$$f_i(z) = Ae^{-jk_z z} + Be^{jk_z z}. \quad (\text{A.20})$$

After applying the boundary conditions

$$\left. \frac{df_i(z)}{dz} \right|_{z=0, z=L} = 0, \quad (\text{A.21})$$

we obtain the following equations for A and B ,

$$\begin{aligned} A(-jk_z) + B(jk_z) &= 0, \\ Ae^{-jk_z L}(-jk_z) + Be^{jk_z L}(jk_z) &= 0. \end{aligned} \quad (\text{A.22})$$

We can conclude that,

$$A = B, k_z = \frac{k\pi}{L}, \quad (\text{A.23})$$

and

$$f_i(z) = C \cos\left(\frac{k\pi}{L} z\right). \quad (\text{A.24})$$

Introducing Eq. (A.18) into Eq. (A.17) yields

$$\frac{\nabla^2 \phi_i(r, \varphi)}{\phi_i(r, \varphi)} + k_i^2 - k_z^2 = 0, \quad (\text{A.25})$$

or

$$\nabla^2 \phi_i(x, y) + (k_i^2 - k_z^2) \phi_i(x, y) = 0. \quad (\text{A.26})$$

We define the wave number k_{mn} by

$$k_{mn}^2 = k_i^2 - k_z^2, \quad (\text{A.27})$$

and spell out the Laplace operator in Eq. (A.26) in cylindrical coordinates to obtain

$$\frac{1}{r} \frac{\partial}{\partial r} \left(r \frac{\partial \phi}{\partial r} \right) + \frac{1}{r^2} \frac{\partial^2 \phi}{\partial \varphi^2} + k_{mn}^2 \phi = 0, \quad (\text{A.28})$$

or

$$\frac{\partial^2 \phi}{\partial r^2} + \frac{1}{r} \frac{\partial \phi}{\partial r} + \frac{1}{r^2} \frac{\partial^2 \phi}{\partial \varphi^2} + k_{mn}^2 \phi = 0. \quad (\text{A.29})$$

Separating the variables further with $\phi(r, \varphi) = R(r)\Psi(\varphi)$, allows us to write Eq. (A.29) as

$$\Psi \frac{\partial^2 R}{\partial r^2} + \frac{\Psi}{r} \frac{\partial R}{\partial r} + \frac{R}{r^2} \frac{\partial^2 \Psi}{\partial \varphi^2} + k_{mn}^2 R\Psi = 0. \quad (\text{A.30})$$

Division by $\phi(r, \varphi) = R(r)\Psi(\varphi)$ leads to

$$\frac{1}{R} \frac{\partial^2 R}{\partial r^2} + \frac{1}{Rr} \frac{\partial R}{\partial r} + \frac{1}{r^2 \Psi} \frac{\partial^2 \Psi}{\partial \varphi^2} + k_{mn}^2 = 0. \quad (\text{A.31})$$

This can be separated into two individual ODEs for the functions $R(r)$ and $\Psi(\varphi)$

$$\begin{aligned} \frac{\partial^2 \Psi}{\partial \varphi^2} + m^2 \Psi &= 0, \\ \frac{1}{r} \frac{d}{dr} \left(r \frac{dR}{dr} \right) + \left(k_{mn}^2 - \frac{m^2}{r^2} \right) R &= 0. \end{aligned} \quad (\text{A.32})$$

Their solutions are

$$\begin{aligned} \Psi(\varphi) &= c e^{jm\varphi}, \\ R(r) &= A J_m(k_{mn} r) + B Y_m(k_{mn} r). \end{aligned} \quad (\text{A.33})$$

Due to the singularity of Y_m at $r=0$, we can conclude that $B=0$, and then we get

$$\begin{aligned} \Psi(\varphi) &= c e^{jm\varphi}, \\ R(r) &= A J_m(k_{mn} r). \end{aligned} \quad (\text{A.34})$$

An (implicit) expression for k_{mn} can be obtained from the boundary condition

$$\left. \frac{dJ_m(k_{mn} r)}{dr} \right|_{r=a} = 0. \quad (\text{A.35})$$

Therefore,

$$\phi = R\Psi = A J_m(k_{mn} r) e^{jm\varphi}, \quad (\text{A.36})$$

$$\psi_i(\vec{r}) = \phi_i(x, y) f_i(z) = A J_m(k_{mn} r) e^{jm\varphi} \cos\left(\frac{k\pi}{L} z\right), \quad (\text{A.37})$$

$$\Gamma_i = \int R\Psi f R^* \Psi^* f^* dv = A^2 \int_0^a r R^2 dr \int_0^{2\pi} d\varphi \int_0^L \cos^2\left(\frac{k\pi}{L} z\right) dz = A^2 \frac{\pi L}{\varepsilon_k} \left(r^2 - \frac{m^2}{k_{mn}^2} \right) J_m^2(k_{mn} r) \Big|_0^a. \quad (\text{A.38})$$

The following expression for \hat{G} is then obtained,

$$\hat{G} = \sum_i \frac{-\psi_i(\vec{r}) \psi_i^*(\vec{r}')}{(k_0^2 - k_i^2) \Gamma_i} = - \sum_m \sum_n \sum_k \frac{J_m(k_{mn} r) e^{jm\varphi} \cos\left(\frac{k\pi}{L} z\right) J_m(k_{mn} r') e^{-jm\varphi'} \cos\left(\frac{k\pi}{L} z'\right)}{(k_0^2 - k_i^2) \frac{\pi L}{\varepsilon_k} \left(r^2 - \frac{m^2}{k_{mn}^2} \right) J_m^2(k_{mn} r) \Big|_0^a}. \quad (\text{A.39})$$

Performing an inverse Fourier transform on Eq. (A.39) yields

$$\begin{aligned}
G(\vec{r}, \vec{r}', t - t') &= \frac{1}{2\pi} \int_{-\infty}^{+\infty} \hat{G} e^{j\omega(t-t')} d\omega \\
&= \frac{1}{2\pi} \int_{-\infty}^{+\infty} - \sum_m \sum_n \sum_k \frac{J_m(k_{mn} r) e^{jm\phi} \cos(\frac{k\pi}{L} z) J_m(k_{mn} r') e^{-jm\phi'} \cos(\frac{k\pi}{L} z')}{(k_0^2 - k_i^2) \frac{\pi L}{\varepsilon_k} (r^2 - \frac{m^2}{k_{mn}^2}) J_m^2(k_{mn} r)} \Big|_0^a e^{j\omega(t-t')} d\omega.
\end{aligned} \tag{A.40}$$

This can be simplified with the residue theorem,

$$G(\vec{r}, \vec{r}', t - t') = \sum_m \sum_n \sum_k g_{mnk}(\vec{r}, \vec{r}') \left(\frac{e^{j\omega_{mnk}(t-t')}}{2} - \frac{e^{-j\omega_{mnk}(t-t')}}{2} \right), \tag{A.41}$$

where

$$g_{mnk}(\vec{r}, \vec{r}') = c_0^2 \frac{J_m(k_{mn} r) e^{jm\phi} \cos(\frac{k\pi}{L} z) J_m(k_{mn} r') e^{-jm\phi'} \cos(\frac{k\pi}{L} z')}{j\omega_{mnk} \frac{\pi L}{\varepsilon_k} (r^2 - \frac{m^2}{k_{mn}^2}) J_m^2(k_{mn} r)} \Big|_0^a. \tag{A.42}$$

Appendix B. Derivation of the integral governing equation for the velocity potential

This derivation begins with the governing equation for the Green's function and the acoustic analogy equation,

$$\frac{1}{c_0^2} \frac{\partial^2 G}{\partial t^2} - \nabla^2 G = \delta(\vec{r} - \vec{r}') \delta(t - t'), \tag{B.1}$$

$$\frac{1}{c^2} \frac{\partial^2 \phi}{\partial t^2} - \nabla^2 \phi = -\frac{\gamma-1}{c^2} q'(\vec{r}, t). \tag{B.2}$$

We change the independent variables from \vec{r}, t to \vec{r}', t' , and exploit the reciprocity of the Green's function,

$$\frac{1}{c_0^2} \frac{\partial^2 G}{\partial t'^2} - \nabla^2 G = \delta(\vec{r} - \vec{r}') \delta(t - t'), \tag{B.3}$$

$$\frac{1}{c^2} \frac{\partial^2 \phi}{\partial t'^2} - \nabla^2 \phi = -\frac{\gamma-1}{c^2} q'(\vec{r}', t'). \tag{B.4}$$

Multiplication of Eq. (B.3) by $\phi(\vec{r}', t')$ and Eq. (B.4) by $G(\vec{r}, \vec{r}', t - t')$ yields

$$\phi(\vec{r}', t') \delta(\vec{r}' - \vec{r}) \delta(t' - t) = -\frac{\gamma-1}{c_0^2} q'(\vec{r}', t') G(\vec{r}, \vec{r}', t - t') + \frac{1}{c_0^2} \left(\phi \frac{\partial^2 G}{\partial t'^2} - G \frac{\partial^2 \phi}{\partial t'^2} \right) - (\phi \nabla^2 G - G \nabla^2 \phi). \tag{B.5}$$

Integrating Eq. (B.5), we obtain

$$\begin{aligned}
& \iint \phi(\vec{r}', t') \delta(\vec{r}' - \vec{r}) \delta(t' - t) d\vec{r}' dt' \\
&= -\frac{\gamma-1}{c_0^2} \iint q'(\vec{r}', t') G(\vec{r}, \vec{r}', t-t') d\vec{r}' dt' + \frac{1}{c_0^2} \iint \left(\phi \frac{\partial^2 G}{\partial t'^2} - G \frac{\partial^2 \phi}{\partial t'^2} \right) d\vec{r}' dt' - \iint (\phi \nabla^2 G - G \nabla^2 \phi) d\vec{r}' dt'. \tag{B.6}
\end{aligned}$$

The third term on the right-hand side of Eq. (B.6) can be simplified with Green's second identity,

$$\iint (\phi \nabla^2 G - G \nabla^2 \phi) d\vec{r}' dt' = \iint \left(\phi \frac{\partial G}{\partial \vec{n}} - G \frac{\partial \phi}{\partial \vec{n}} \right) ds' dt' = 0. \tag{B.7}$$

The second term on the right-hand side of Eq. (B.6) can be simplified by direct integration with respect to t' and subsequently applying the causality principle of the Green's function,

$$\iint \left(\phi \frac{\partial^2 G}{\partial t'^2} - G \frac{\partial^2 \phi}{\partial t'^2} \right) d\vec{r}' dt' = \iint \frac{\partial}{\partial t'} \left(\phi \frac{\partial G}{\partial t'} - G \frac{\partial \phi}{\partial t'} \right) d\vec{r}' dt' = \int \left(\phi \frac{\partial G}{\partial t'} - G \frac{\partial \phi}{\partial t'} \right) \Big|_0^t d\vec{r}' = - \int \left(\phi \frac{\partial G}{\partial t'} - G \frac{\partial \phi}{\partial t'} \right) \Big|_{t'=0} d\vec{r}'. \tag{B.8}$$

Then Eq. (B.6) can be written as

$$\phi(\vec{r}, t) = -\frac{\gamma-1}{c_0^2} \iint q'(\vec{r}', t') G(\vec{r}, \vec{r}', t-t') d\vec{r}' dt' - \frac{1}{c_0^2} \int \left(\phi \frac{\partial G}{\partial t'} - G \frac{\partial \phi}{\partial t'} \right) \Big|_{t'=0} d\vec{r}'. \tag{B.9}$$

By introducing the initial conditions given in Eq. (13) into Eq. (B.9), we finally obtain

$$\begin{aligned}
\phi(\vec{r}, t) &= -\frac{\gamma-1}{c_0^2} \iint q'(\vec{r}', t') G(\vec{r}, \vec{r}', t-t') d\vec{r}' dt' - \frac{1}{c_0^2} \int (\phi_0 \delta(\vec{r}' - \vec{r}_q) \frac{\partial G}{\partial t'} \Big|_{t'=0}) d\vec{r}' \\
&= -\frac{\gamma-1}{c_0^2} \iint q'(\vec{r}', t') G(\vec{r}, \vec{r}', t-t') d\vec{r}' dt' - \frac{\phi_0}{c_0^2} \frac{\partial G}{\partial t'} \Big|_{\vec{r}'=\vec{r}_q}^{t'=0}. \tag{B.10}
\end{aligned}$$

References

- [1] A.A. Putnam, Combustion driven oscillations in industry, Am. Elsevier Pub. Co (1971).
- [2] L. Crocco, S.I. Cheng, Theory of combustion instability in liquid propellant rocket motors, Изд-Во Иностранная Литература, (1956).
- [3] U.G. Hegde, D. Reuter, B.R. Daniel, B.T. Zinn, Flame driving of longitudinal instabilities in dump type ramjet combustors, Combust. Sci. Technol. 55 (1987) 125–138. <https://doi.org/10.1080/00102208708947075>.
- [4] J.J. Keller, Thermoacoustic Oscillations in Combustion Chambers of Gas Turbines, AIAA J. 33 (1995) 2280–2287.
- [5] T.C. Lieuwen, V. Yang, Combustion instabilities in gas turbine engines: operational experience, fundamental mechanisms, and modeling, American Institute of Aeronautics and Astronautics, 2005.

- [6] S. Candel, Combustion dynamics and control: Progress and challenges, *Proc. Combust. Inst.* 29 (2002) 1–28.
- [7] Y. Huang, V. Yang, Dynamics and stability of lean-premixed swirl-stabilized combustion, *Prog. Energy Combust. Sci.* 35 (2009) 293–364.
- [8] C.O. Paschereit, W. Polifke, Investigation of the thermoacoustic characteristics of a lean premixed gas turbine burner, in: *Turbo Expo Power Land, Sea, Air*, American Society of Mechanical Engineers, 1998: p. V003T06A057.
- [9] F.E.C. Culick, Combustion instabilities in propulsion systems, in: *Unsteady Combust.*, Springer, 1996: pp. 173–241.
- [10] V. Yang, Introductions: stability characteristics and control approach, *Act. Control Engine Dyn. Von Karman Inst. Fluid Dyn.* (2001).
- [11] B. Higgins, On the sound produced by a current of hydrogen gas passing through a tube, *J. of Natural Phil. Chem*, in: *Arts*, 1802.
- [12] P.L. Rijke, LXXI. Notice of a new method of causing a vibration of the air contained in a tube open at both ends, *London, Edinburgh, Dublin Philos. Mag. J. Sci.* 17 (1859) 419–422.
- [13] K.T. Feldman Jr, Review of the literature on Rijke thermoacoustic phenomena, *J. Sound Vib.* 7 (1968) 83–89.
- [14] M. Heckl, Non-linear acoustic effects in the Rijke Tube, *Acoustica* 72 (1990) 63–71.
- [15] R.L. Raun, M.W. Beckstead, J.C. Finlinson, K.P. Brooks, A review of Rijke tubes, Rijke burners and related devices, *Prog. Energy Combust. Sci.* 19 (1993) 313–364. [https://doi.org/10.1016/0360-1285\(93\)90007-2](https://doi.org/10.1016/0360-1285(93)90007-2).
- [16] S.M. Sarpotdar, N. Ananthkrishnan, S.D. Sharma, The Rijke tube—a thermo-acoustic device, *Resonance* 8 (2003) 59–71.
- [17] M.A. Heckl, Active control of the noise from a Rijke tube, *J. Sound Vib.* 124 (1988) 117–133. [https://doi.org/10.1016/S0022-460X\(88\)81408-1](https://doi.org/10.1016/S0022-460X(88)81408-1).
- [18] A.S. Morgans, A.P. Dowling, Model-based control of combustion instabilities, *J. Sound Vib.* 299 (2007) 261–282.
- [19] G.A. de Andrade, R. Vazquez, D.J. Pagano, Boundary feedback control of unstable thermoacoustic oscillations in the Rijke tube, *IFAC-PapersOnLine* 49 (2016) 48–53.
- [20] N.N. Deshmukh, S.D. Sharma, Experiments on heat content inside a Rijke tube with suppression of thermo-acoustics instability, *Int. J. Spray Combust. Dyn.* 9 (2017) 85–101.

- [21] U. Zalluhoglu, N. Olgac, Analytical and experimental study on passive stabilization of thermoacoustic dynamics in a Rijke tube, *J. Dyn. Syst. Meas. Control* 140 (2018) 21007.
- [22] Y. Zhang, L. Huang, Electroacoustic control of Rijke tube instability, *J. Sound Vib.* 409 (2017) 131–144.
- [23] Z. Zhang, D. Zhao, N. Han, S. Wang, J. Li, Control of combustion instability with a tunable Helmholtz resonator, *Aerosp. Sci. Technol.* 41 (2015) 55–62.
- [24] S. Jo, Y. Choi, H.J. Kim, Evaluation of the damping capacity according to the geometric and the number of resonator with thermal environment using a Rijke tube, *Aerosp. Sci. Technol.* 88 (2019) 1–8.
- [25] N.N. Deshmukh, B. Kudachi, S. Joy, S. Phansalkar, V. Pillai, T. Thomas, Suppression of Thermo-Acoustic Instabilities using Helmholtz Resonator, in: 2019 Int. Conf. Nascent Technol. Eng., IEEE, 2019: pp. 1–6.
- [26] D. Zhao, A.S. Morgans, Tuned passive control of combustion instabilities using multiple Helmholtz resonators, *J. Sound Vib.* 320 (2009) 744–757.
- [27] J.F. Bourgouin, D. Durox, J.P. Moeck, T. Schuller, S. Candel, A new pattern of instability observed in an annular combustor: The slanted mode, *Proc. Combust. Inst.* 35 (2015) 3237–3244.
<https://doi.org/10.1016/j.proci.2014.06.029>.
- [28] T. Poinso, Prediction and control of combustion instabilities in real engines, *Proc. Combust. Inst.* 36 (2017) 1–28. <https://doi.org/10.1016/j.proci.2016.05.007>.
- [29] J. Kopitz, A. Huber, T. Sattelmayer, W. Polifke, Thermoacoustic stability analysis of an annular combustion chamber with acoustic low order modeling and validation against experiment, *Proc. ASME Turbo Expo 2* (2005) 583–593. <https://doi.org/10.1115/GT2005-68797>.
- [30] S.R. Stow, A.P. Dowling, A time-domain network model for nonlinear thermoacoustic oscillations, (2009).
- [31] V.S. Acharya, M.R. Bothien, T.C. Lieuwen, Non-linear dynamics of thermoacoustic eigen-mode interactions, *Combust. Flame* 194 (2018) 309–321. <https://doi.org/10.1016/j.combustflame.2018.04.021>.
- [32] J.P. Moeck, C.O. Paschereit, Nonlinear interactions of multiple linearly unstable thermoacoustic modes, *Int. J. Spray Combust. Dyn.* 4 (2012) 1–27.
- [33] A. Orchini, G.A. Mensah, J.P. Moeck, Effects of nonlinear modal interactions on the thermoacoustic stability of annular combustors, *J. Eng. Gas Turbines Power* 141 (2019). <https://doi.org/10.1115/1.4040768>.
- [34] J.G.R. von Saldern, J.P. Moeck, A. Orchini, Nonlinear interaction between clustered unstable thermoacoustic modes in can-annular combustors, *Proc. Combust. Inst.* 38 (2021) 6145–6153.

<https://doi.org/10.1016/j.proci.2020.06.236>.

- [35] A.P. Dowling, Nonlinear self-excited oscillations of a ducted flame, *J. Fluid Mech.* 346 (1997) 271–290.
- [36] N. Noiray, D. Durox, T. Schuller, S. Candel, A unified framework for nonlinear combustion instability analysis based on the flame describing function, *J. Fluid Mech.* 615 (2008) 139–167.
- [37] L. Qin, X. Wang, G. Zhang, X. Sun, Effect of nonlinear flame response on the design of perforated liners in suppression of combustion instability, *J. Sound Vib.* 511 (2021) 116314.
- [38] J.P. Moeck, M. Paul, C.O. Paschereit, Thermoacoustic instabilities in an annular Rijke tube, in: *Turbo Expo Power Land, Sea, Air*, 2010: pp. 1219–1232.
- [39] J.-F. Bourgouin, D. Durox, J.P. Moeck, T. Schuller, S. Candel, Self-sustained instabilities in an annular combustor coupled by azimuthal and longitudinal acoustic modes, in: *Turbo Expo Power Land, Sea, Air*, American Society of Mechanical Engineers, 2013: p. V01BT04A007.
- [40] M. Philip, M. Boileau, R. Vicquelin, T. Schmitt, D. Durox, J.-F. Bourgouin, S. Candel, Ignition sequence of an annular multi-injector combustor, *Phys. Fluids* 26 (2014).
- [41] D. Durox, K. Prieur, T. Schuller, S. Candel, Different flame patterns linked with swirling injector interactions in an annular combustor, *J. Eng. Gas Turbines Power* 138 (2016) 101504.
- [42] J.-F. Bourgouin, D. Durox, J.P. Moeck, T. Schuller, S. Candel, Characterization and modeling of a spinning thermoacoustic instability in an annular combustor equipped with multiple matrix injectors, *J. Eng. Gas Turbines Power* 137 (2015) 21503.
- [43] G. Vignat, D. Durox, A. Renaud, S. Candel, High amplitude combustion instabilities in an annular combustor inducing pressure field deformation and flame blow off, *J. Eng. Gas Turbines Power* 142 (2020) 11016.
- [44] Y. Fang, Y. Yang, K. Hu, G. Wang, J. Li, Y. Zheng, Experimental study on self-excited thermoacoustic instabilities and intermittent switching of azimuthal and longitudinal modes in an annular combustor, *Phys. Fluids* 33 (2021).
- [45] C. Ye, G. Wang, Y. Fang, C. Ma, Ignition dynamics in annular combustor with turbine guide vanes, *J. Combust. Sci. Technol* 26 (2020) 75–80.
- [46] M. Shahi, J.B.W. Kok, J.C.R. Casado, A.K. Pozarlik, Transient heat transfer between a turbulent lean partially premixed flame in limit cycle oscillation and the walls of a can type combustor, *Appl. Therm. Eng.* 81 (2015) 128–139.

- [47] C.A. Armitage, R. Balachandran, E. Mastorakos, R.S. Cant, Investigation of the nonlinear response of turbulent premixed flames to imposed inlet velocity oscillations, *Combust. Flame* 146 (2006) 419–436.
- [48] M. Talei, E.R. Hawkes, M.J. Brear, A direct numerical simulation study of frequency and Lewis number effects on sound generation by two-dimensional forced laminar premixed flames, *Proc. Combust. Inst.* 34 (2013) 1093–1100.
- [49] H. Wang, K. Luo, F. Yi, J. Fan, Analysis of flame characteristics in a laboratory-scale turbulent lifted jet flame via DNS, *Int. J. Spray Combust. Dyn.* 5 (2013) 225–242.
- [50] T. Poinsot, S. Candel, A. Trouvé, Applications of direct numerical simulation to premixed turbulent combustion, *Prog. Energy Combust. Sci.* 21 (1995) 531–576.
- [51] L.Y.M. Gicquel, G. Staffelbach, T. Poinsot, Large eddy simulations of gaseous flames in gas turbine combustion chambers, *Prog. Energy Combust. Sci.* 38 (2012) 782–817.
- [52] G. Boudier, N. Lamarque, G. Staffelbach, L.Y.M. Gicquel, T. Poinsot, Thermo-acoustic stability of a helicopter gas turbine combustor using large eddy simulation, *Int. J. Aeroacoustics* 8 (2009) 69–93.
- [53] H.J. Krediet, C.H. Beck, W. Krebs, S. Schimek, C.O. Paschereit, J.B.W. Kok, Identification of the flame describing function of a premixed swirl flame from LES, *Combust. Sci. Technol.* 184 (2012) 888–900.
- [54] S. Hermeth, G. Staffelbach, L.Y.M. Gicquel, T. Poinsot, LES evaluation of the effects of equivalence ratio fluctuations on the dynamic flame response in a real gas turbine combustion chamber, *Proc. Combust. Inst.* 34 (2013) 3165–3173.
- [55] H.J. Krediet, C.H. Beck, W. Krebs, J.B.W. Kok, Saturation mechanism of the heat release response of a premixed swirl flame using LES, *Proc. Combust. Inst.* 34 (2013) 1223–1230.
- [56] J.-F. Parmentier, P. Salas, P. Wolf, G. Staffelbach, F. Nicoud, T. Poinsot, A simple analytical model to study and control azimuthal instabilities in annular combustion chambers, *Combust. Flame* 159 (2012) 2374–2387.
- [57] M. Bauerheim, J.-F. Parmentier, P. Salas, F. Nicoud, T. Poinsot, An analytical model for azimuthal thermoacoustic modes in an annular chamber fed by an annular plenum, *Combust. Flame* 161 (2014) 1374–1389.
- [58] S. Evesque, W. Polifke, Low-order acoustic modelling for annular combustors: validation and inclusion of modal coupling, in: *Turbo Expo Power Land, Sea, Air, 2002*: pp. 321–331.
- [59] D. You, V. Yang, X. Sun, Three-Dimensional Linear Stability Analysis of Gas Turbine Combustion Dynamics,

Progress in Astronautics and Aeronautics 210 (2005) 415–443.

- [60] L. Li, X. Sun, Effect of vorticity waves on azimuthal instabilities in annular chambers, *Combust. Flame* 162 (2015) 628–641.
- [61] G. Zhang, X. Wang, L. Li, X. Sun, Effects of perforated liners on controlling combustion instabilities in annular combustors, *AIAA Journal* 58 (2020) 3100–3114.
- [62] A. Bigongiari, M. Heckl, Analysis of the interaction of thermoacoustic modes with a Green’s function approach, *Int. J. Spray Combust. Dyn.* 10 (2018) 326–336. <https://doi.org/10.1177/1756827718809570>.
- [63] M.A. Heckl, Analytical model of nonlinear thermo-acoustic effects in a matrix burner, *J. Sound Vib.* 332 (2013) 4021–4036. <https://doi.org/10.1016/j.jsv.2012.11.010>.
- [64] A. Bigongiari, M.A. Heckl, A Green’s function approach to the rapid prediction of thermoacoustic instabilities in combustors, *J. Fluid Mech.* 798 (2016) 970–996. <https://doi.org/10.1017/jfm.2016.332>.
- [65] M.A. Heckl, M.S. Howe, The Rijke tube: Green’s function approach in the time and frequency domain, in: *Proc. 14th Int. Congr. Sound Vib. Cairns, Aust., 2007*: pp. 9–12.
- [66] J.W.S.B. Rayleigh, *The theory of sound*, Macmillan, 1896.